Quaternary Science Reviews 299 (2023) 107869

Contents lists available at ScienceDirect

Quaternary Science Reviews

journal homepage: www.elsevier.com/locate/quascirev

Variations in Asian summer monsoon and hydroclimate during Heinrich stadials 4 revealed by stalagmite stable isotopes and trace elements

Yao Wu [a, b, c, 1], Ting-Yong Li [a, 1, *], Jun-Yun Li [b, **], Hai Cheng [d], You-Feng Ning [d], Chuan-Chou Shen [e, f], Yan Yang [b], Jing-Yao Zhao [d], Chao-Jun Chen [a], Ming-Qiang Liang [g], Si-Ya Xiao [b], Hai-Ying Qiu [b], Yu-Zhen Xu [b], Yang-Yang Huang [b], Tsai-Luen Yu [e, h], R. Lawrence Edwards [i]

[a] Yunnan Key Laboratory of Plateau Geographical Processes & Environmental Changes, Faculty of Geography, Yunnan Normal University, Kunming, 650500, China
[b] Chongqing Key Laboratory of Karst Environment, School of Geographical Sciences, Southwest University, Chongqing, 400715, China
[c] Institute of Environmental Physics, Heidelberg University, Heidelberg, 69120, Germany
[d] Institute of Global Environmental Change, Xi'an Jiaotong University, Xi'an, 710049, China
[e] High-Precision Mass Spectrometry and Environment Change Laboratory (HISPEC), Department of Geosciences, National Taiwan University, Taipei, 10617, Taiwan, ROC
[f] Research Center for Future Earth, National Taiwan University, Taipei, 10617, Taiwan, ROC
[g] Georges Lemaître Center for Earth and Climate Research, Earth and Life Institute, Université Catholique de Louvain, Louvain-la-Neuve, 1348, Belgium
[h] Marine Industry and Engineering Research Center, National Academy of Marine Research, Kaohsiung, 806, Taiwan, ROC
[i] Department of Earth Sciences, University of Minnesota, Minneapolis, MN, USA

A R T I C L E I N F O

Article history:
Received 9 May 2022
Received in revised form
27 October 2022
Accepted 7 November 2022
Available online 25 November 2022

Keywords:
Stalagmite $\delta^{18}O$
Heinrich stadials 4
Asian summer monsoon
Trace elements
Spatial difference of hydroclimate

A B S T R A C T

The iceberg melting-induced Heinrich events (HEs), which were first reported in 1988, caused a series of centennial-millennial global climate changes during the last glacial period. The patterns and details of low-latitude monsoons, oceans, and atmospheric circulation responses to HEs still need to be understood. Here, we report 11a resolved $\delta^{13}C$, $\delta^{18}O$ and 36a resolved Mg/Ca, Sr/Ca and Ba/Ca multi-proxy stalagmite records during 42.29–37.14 ka BP from Yangkou cave, southwestern China. The Greenland ice cores and the $\delta^{18}O$ of stalagmites from northern China recorded a rapid onset/termination of Heinrich stadials (HS) 4 (~0.2 ka). However, the transition interval for the weakening/strengthening of the Asian summer monsoon (ASM) during HS4, as recorded by the southern Chinese stalagmite $\delta^{18}O$, is about 0.5 ka. Low latitude monsoons and hydrological variations are influenced by tropical oceans and interhemispheric thermal contrasts, which prolong the onset/termination transition process of HS4. Our findings highlight the importance of atmosphere-ocean interactions at low latitudes and in the Southern Hemisphere for ASM dynamics, which triggered the termination of millennial-scales abrupt climate events. During HS4, variations of the $\delta^{13}C$ and trace elements ratios are inconsistent with $\delta^{18}O$, indicating that while the ASM is weakened, regional hydroclimate and local ecology are not significantly degraded, resulting in a relatively moderate hydrological environment. Prolonged southerly subtropical westerlies, super El Niño Southern Oscillation, western China autumn rains, and lower regional evaporation, may increase regional precipitation in different seasons and regulate hydrological conditions during HS4. As a result, while the ASM has weakened, regional hydrological conditions in the Yangtze River basin in southwest China maintain wet environmental conditions. The gradual northward shift of the Intertropical Convergence Zone and subtropical westerlies during the latter phase of HS4 will cause a limited northward shift of the rainfall bands. Although regional hydrological conditions deteriorate slightly in comparison to the early phase, it remains humid overall. We present new evidence that local

* Corresponding author.
** Corresponding author.
E-mail addresses: cdlty@swu.edu.cn, cdlty@163.com (T.-Y. Li), jxljy@swu.edu.cn (J.-Y. Li).
[1] Both authors contributed equally to this work.

https://doi.org/10.1016/j.quascirev.2022.107869
0277-3791/© 2022 Elsevier Ltd. All rights reserved.

hydrological conditions and ASM intensity were not fully coupled during the abrupt climate events on millennial scales in the last glacial period.

© 2022 Elsevier Ltd. All rights reserved.

1. Introduction

During the last glacial period, six abrupt climate events correspond to abrupt increases in ice-rafted detritus (IRD) in the North Atlantic. These episodes are associated with ice sheet melting and are accompanied by large shifts of oxygen stable isotopes preserved in North Atlantic deep-sea sediments, known as Heinrich events (HEs) (Heinrich, 1988; Broecker et al., 1992; Hemming, 2004; Andrews and Voelker, 2018). The entire cold interval, associated with HEs are termed as Heinrich stadials (HS) (Barker et al., 2009). Sea surface temperature (SST) in the North Atlantic decreased significantly during the HS, coinciding with climate fluctuations recorded in Greenland ice core δ^{18}O records (Belen et al., 2007; Guillevic et al., 2013; Gkinis et al., 2021). The impact of HS profoundly affected climate in both the Northern and Southern Hemispheres (NH, SH) through the Atlantic meridional overturning circulation (AMOC), the bipolar seesaw, and atmospheric circulations (Pausata et al., 2011; Zhang et al., 2017; Ziemen et al., 2019; Skinner et al., 2020).

Recent research has provided a series of high-resolution stalagmites paleoclimate records defining the onset/termination timings of HS4 and discussed the mechanisms of global climate change (Cheng et al., 2021; Zhang et al., 2021d). HS4 is recorded in stalagmites that respond to changes in the Asian summer monsoon (ASM) lasting 1.86 ka (40.20 ± 0.08–38.34 ± 0.07 ka BP) (Cheng et al., 2021). High-resolution stalagmite δ^{18}O records from Southeast China indicate that the onset and initial termination of HS4 can be observed at 40.04 ± 0.07 and 37.76 ± 0.05 ka BP, and are significantly offset from other stalagmite records in the ASM area (Zhang et al., 2021d). The onset of the HS4 in South American Monsoon (SAM) is consistent with ASM (40.19 ± 0.05 ka BP), but the termination of HS4 is earlier than ASM (38.85 ± 0.11 ka BP) (Wendt et al., 2019; Cheng et al., 2021; Zhang et al., 2021d). Salinity variations of the Amazon Plume Region (Liang et al., 2020; Cheng et al., 2021), atmospheric moisture transport in Central America influenced by atmospheric CO_2 concentration (Zhang et al., 2017), the Intertropical Convergence Zone (ITCZ) shift (Guillevic et al., 2014), tropical Pacific SST (Carolin et al., 2013), and SH Westerlies shift (Menviel et al., 2018), all suggest low latitude and SH trigger for the termination of HS4. This climate change signals then propagated northward towards the North Atlantic high latitudes, as AMOC became activated (Cheng et al., 2021; Zhang et al., 2021d).

Inconsistent paleoclimate patterns between high and low latitudes are evident in HS1-HS3 (Dong et al., 2022; Li et al., 2021a), Younger Dryas (YD) (Partin et al., 2015; Zhang et al., 2021a), and some Greenland interstadial (GI) events (Guillevic et al., 2014; Duan et al., 2016a; Li et al., 2017; Zhang et al., 2021c). During HS4, the processes of climate change are not always consistent between high and low latitudes (Guillevic et al., 2014; Wendt et al., 2019; Cheng et al., 2021; Zhang et al., 2021d). For example, abrupt changes in monsoon circulation at low latitudes, including the ASM and SAM, have occurred while Greenland temperatures remained stable during HS4 (Cheng et al., 2021; Zhang et al., 2021d). The southward shift of the ITCZ at the onset of HS4 lagged the onset of Greenland cooling by 550 ± 60 years (Guillevic et al., 2014). These differences in paleoclimate records dated with high-precision are not entirely attributable to chronological errors but instead suggest different climatic responses to IRD events in the North Atlantic and elsewhere (Hemming, 2004; Belen et al., 2007; Andrews and Voelker, 2018; Bradley and Diaz, 2021).

Recent research indicates that the low-latitude ASM undergoes a more gradual weakening/strengthening process than the Greenland ice core δ^{18}O during HS4 (Cheng et al., 2021; Zhang et al., 2021d), but the climate dynamics mechanisms underlying this difference have not been thoroughly discussed. The general signature of climate change in the ASM and the Western Pacific warm pool (WPWP) during the last glacial period provides the key to understanding the driving factors responsible (Huang et al., 2019; Liu et al., 2022). The interaction between the low latitude monsoon, tropical ocean-atmosphere coupling, and the role of the Southern Ocean should be considered.

The stalagmites δ^{18}O provide an excellent proxy for exploring the ASM dynamics during the HS (Cheng et al., 2021; Li et al., 2021a; Zhang et al., 2021d; Dong et al., 2022). However, current paleoclimate reconstructions of the Asian monsoon region rarely offer comprehensive evidence of environmental change during the HS, especially for evaluating the relationship between regional hydrological conditions (e.g., precipitation and dry-wet) and ASM intensity. The response of dry-wet changes in the hydrological environment to climate change is inconsistent across China (Zhang et al., 2018, 2021b; Liu et al., 2019a, b; He et al., 2021a; Zhao et al., 2021a). For example, during Termination 1, while the East Asian summer monsoon (EASM) weakened during YD and HS1, east-central China is in wetter conditions because of the prolonged Meiyu (Zhang et al., 2018). The decoupling of the ITCZ and the subtropical westerlies resulted in a more pronounced dry-wet transition in the hydrological environment in southern China during the Mystery Interval (17.5–14.5 ka BP) compared to the higher latitudes (Zhao et al., 2021a). A recent study systematically evaluated the potential for decoupling between region precipitation and monsoon intensity within East Asia during the Holocene (Zhang et al., 2021b). The results proved that the relationship between EASM intensity and precipitation is non-homogeneous in East Asia (Zhang et al., 2021b). Variations in the monsoon rainfall bands under the control of climatic factors such as subtropical westerlies (Zhang et al., 2018; Chiang et al., 2020), ITCZ (McGee et al., 2014, 2018), and Western Pacific Subtropical High (WPSH) lead to an anti-phase of precipitation in the north and south of China (Ding et al., 2018). Because of the complexity of the factors influencing atmospheric precipitation δ^{18}O ($\delta^{18}O_p$) of ASM (Ruan et al., 2019; He et al., 2021b; Zhang et al., 2021b), other proxies sensitive to hydrological conditions are necessary to reconstruct the regional environmental response to climate change and to evaluate the coupling between local hydrological conditions and ASM intensity.

Stalagmite δ^{13}C and trace elements are becoming critical as proxies for the paleoenvironment variation due to their ability to record high-resolution changes in the environment, especially hydrological processes (Fohlmeister et al., 2020; Jia et al., 2022; Liang et al., 2022; Wang et al., 2022b). The results of cave monitoring and paleoenvironmental reconstruction in China indicate that the changes of δ^{13}C, Ca, Sr, Mg, Ba, and their ratios (X/Ca) in stalagmites are mainly influenced by organic (biological activity, vegetation change, etc.) and inorganic processes (e.g. prior calcite precipitation (PCP)) (Fairchild and Treble, 2009; Chen and Li, 2018; Li et al., 2018;

Yin et al., 2021), which can reconstruct the variation of regional environmental (temperature, precipitation, etc.) (Liu et al., 2019b; Xue et al., 2021; Liang et al., 2022). During the transport of these geochemical indicators through the epikarst zone, influenced by various climatic and interior cave environments, the climatic signals they carried are often modified, reflecting the mixture of climatic and non-climatic factors (Cosford et al., 2009; Fairchild and Treble, 2009; Fohlmeister et al., 2020). The comparison of multiple proxies in stalagmites will be helpful in the comprehensive reconstruction of the environment variations and provide new insight into the interpretation of stalagmites $\delta^{18}O$.

Here, we present a $\delta^{18}O$ record from a precisely dated and annual laminae counted stalagmite from Yangkou cave in southwest China. This record provides a high-resolution (11a) reconstruction of ASM variation during 42.29–37.14 ka BP. The reasons for the differences in climate change (abrupt or gradual) between the North Atlantic and low latitudes during the onset and termination of HS4 are discussed. Combined with the $\delta^{13}C$ and trace element (Mg, Sr, Ba) records, we comprehensively reconstructed the processes of variation in the hydrological environment of southwest China during the HS4. Our study provides new evidence that local hydroclimate in the Asian monsoon region is not fully coupled with monsoon intensity, contributing to a better understanding of the regional hydro-environmental response to millennial-scales climate events in the last glacial period.

2. Material and methods

2.1. Yangkou cave and YK1 stalagmite

Yangkou cave (29°02′N, 107°11′ E, 2140 m a.s.l.) is located in the Permian limestones of Jinfo mountain, Chongqing, southwest China (Fig. 1). The corridor-shaped cave is 2245 m long, 15–20 m wide, and 8–12 m high (Figure S1) (Chen and Li, 2018). The region has a subtropical humid monsoon climate, affected by the East Asian and Indian summer monsoons. The mean annual temperature and precipitation are 8.5 °C and 1400 mm. April–October precipitation accounts for 83% of the annual precipitation (Chen and Li, 2018) (Figure S2).

Monitoring data indicate that the annual average temperature in the cave is 7.5 °C, and the response of cave drip to external climate and environmental changes lag by no more than three months (Chen and Li, 2018) (Figure S2). The YK1 stalagmite used in this study is composed of dense calcite with obvious lamina (Fig. 2a). The YK1 stalagmite is 630 mm long. We focused on the section from 529 to 630 mm in this study.

2.2. Methods

2.2.1. ^{230}Th dating

On the polished surface of YK1, 50–100 mg powder subsamples were collected for U–Th dating. A total of 15 U–Th dating subsamples were drilled from 529 to 630 mm in depth from stalagmite YK1 (Fig. 2a). The U and Th were separated using the standard chemical procedures described by Edwards et al. (1987), Shen et al. (2012), and Cheng et al. (2013). The ^{230}Th dating was conducted in the High-precision Mass Spectrometry and Environment Change Laboratory (HISPEC) of National Taiwan University (5/15) and the Isotope Laboratory of the Institute of Global Environmental Change of Xi'an Jiaotong University (10/15) using a Neptune multi-collector inductively coupled plasma mass spectrometer (MC-ICP-MS). The decay constants used for ^{230}Th, ^{234}U, and ^{238}U are 9.1705×10^{-6} yr^{-1}, 2.82206×10^{-6} yr^{-1} (Cheng et al., 2013), and 1.55125×10^{-10} yr^{-1} (Jaffey et al., 1971), respectively. The age correction for the initial ^{230}Th was performed using the average crustal $^{230}Th/^{232}Th$ ratio of $4.4 \pm 2.2 \times 10^{-6}$ (Taylor and Mclennan, 1995).

2.2.2. Stable isotopes analyses

On the polished section of YK1, 489 stable isotope samples were drilled using a Micromill at a resolution of 0.2 mm along the growth axis from 529 to 630 mm. Stable isotope analyses were performed using a Perspective isotope ratio mass spectrometer (IRMS), combined with a Nu Carb automated carbonate device at Beijing Createch Testing Technology Co., Ltd, China. Results are reported with respect to Vienna Pee Dee Belemnite (V-PDB). The one-sigma

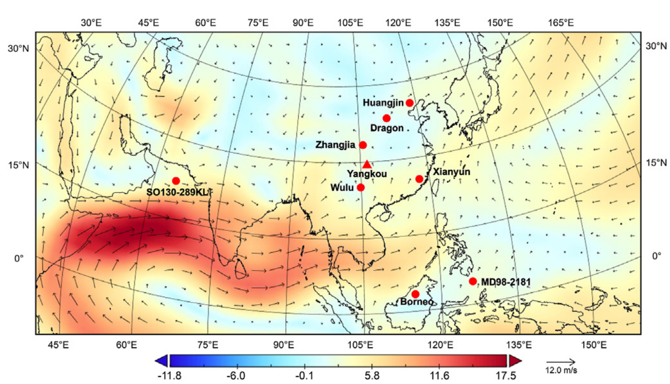

Fig. 1. Study sites and general circulation pattern of the ASM. Arrows indicate the summer (June–August) 850 hPa wind field. Wind data are derived from NCEP/NCAR reanalysis datasets (Kalnay et al., 1996), with averages calculated over the period from 1981 to 2020. The red triangle shows the location of Yangkou cave (This study), the red dots show the locations of Dragon cave (Dong et al., 2018), Huangjin cave (Liang et al., 2022), Zhangjia cave (Cheng et al., 2021), Wulu cave (Cheng et al., 2021), Xianyun cave (Zhang et al., 2021d), Borneo cave (Carolin et al., 2013), Western Pacific Warm Pool core MD98-2181 (Saikku et al., 2009) and Arabian Sea sediment core SO130-289 KL (Deplazes et al., 2013). (For interpretation of the references to colour in this figure legend, the reader is referred to the Web version of this article.)

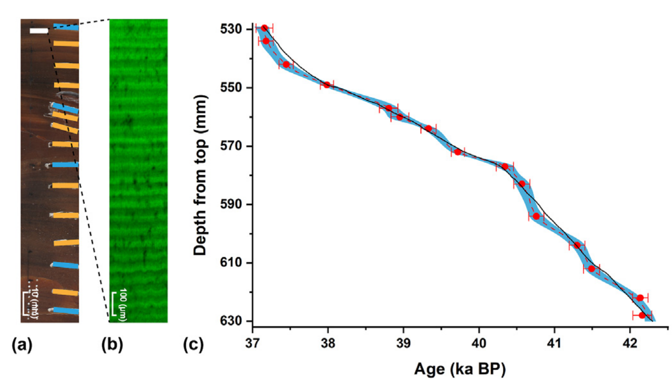

Fig. 2. Age model of YK1 stalagmite . **(a)** A polished slab of stalagmite YK1 (529–630 mm). Blue and orange bars indicate the positions of the 15 samples collected for U–Th dating used to construct the chronology. The dating of the blue samples was performed at the High-precision Mass Spectrometry and Environment Change Laboratory (HISPEC) of National Taiwan University. The dating of the orange samples was performed at the Isotope Laboratory of the Institute of Global Environmental Change of Xi'an Jiaotong University. **(b)** A magnified figure of the fluorescence profile of the YK1 stalagmite (white band in a). **(c)** Age model of stalagmite YK1. The red dots are the depths and ages of the U–Th dating samples, and the error bars indicate the dating error (±2σ). The black line indicates the YK1 stalagmite age model based on fluorescence laminae counts. The red dashed line is a COPRA age model for YK1, the blue band indicates the 95% confidence limit (Breitenbach et al., 2012). The COPRA age model is consistent with fluorescence laminae counts results within error. (For interpretation of the references to colour in this figure legend, the reader is referred to the Web version of this article.)

external error is < ±0.1‰ and < ±0.06‰ for $\delta^{18}O$ and $\delta^{13}C$, respectively.

Here, we use the RAMPFIT algorithm to identify the onset and termination of HS4 in stalagmite and ice core records (Mudelsee, 2000). The RAMPFIT uses a combination of weighted least squares and brute force search to estimate the break regression parameters, considering features such as the sequence dependence and temporal resolution difference of paleoclimate records (Mudelsee, 2000). The validity of this method has been proven in numerous previous studies (Jiang et al., 2014; Zhang et al., 2021d). The identification of mutation points requires the provision of a fitting interval containing breakpoints. To avoid as much subjectivity in the choice of the fitting interval as possible, we used the same time interval for paleoclimate records from the same region and the results of the analysis are reported in Table S1. All results are visually inspected and agree with the actual process of transition of the individual paleoclimate records at the onset and termination of HS4.

2.2.3. Trace elements analyses

On the polished surface of YK1, ~10 mg powder subsamples were collected for trace elements. A total of 147 samples were obtained from YK1 stalagmites sampled at a resolution of 0.5 mm from 529 to 574 mm depth and a resolution of 1 mm from 574 to 630 mm. The sample was dissolved using purified 5% HNO_3. After complete dissolution, the sample was fixed to 10 ml using deionized water and transferred to a centrifuge tube for measurement. Measurements of trace elements of YK1 were completed at the Chongqing Key Laboratory of Karst Environment, Southwest University, using an Inductively coupled plasma - optical emission spectrometry (ICP-OES). Trace elements measured included Ca, Mg, Ba and Sr with a lower limit of detection of 0.001 mg/L and a relative standard deviation of <2.0%.

2.2.4. Stalagmite laminae counting

The fluorescence of the laminae was scanned using a Nikon A1 laser scanning confocal microscope at the State key laboratory for manufacturing systems engineering, Xi'an Jiaotong University. A 101 mm (529–630 mm) fluorescence image of the stalagmite was obtained along the growth axis on the polished profile (Fig. 2b). Detailed methods and settings are described in Zhao and Cheng (2017). Three paths were selected for annual layer counting along the stalagmite growth axis and 1 mm away from both sides of the growth axis. The final number of annual layers is the average of the results of three paths.

3. Results

3.1. Age model

The fifteen measured ^{230}Th dates are in stratigraphic order (Table S2; Fig. 2c). The ages of the top and bottom samples were 37.16 ka BP and 42.16 ka BP, respectively (Table S2). The average 2σ dating error of ±0.10 ka is < 3.0‰, which provides precise chronological control.

The fluorescence laminae in stalagmites are the result of the seasonal transport of soil organic matter, Fe, Al, Si and other mineral elements on an interannual time scales to the cave drip and formed during the deposition of the stalagmite (Tan et al., 2006). Combining YK1 stalagmite fluorescence images, we counted pairs of fluorescent and dark layers as annual layers, accumulating them sequentially. Fluorescence laminae counts along three paths in this interval were composed of 5096, 5171, and 5160 bands, with an average of 5140 ± 41 bands. The number of counted bands matches the radiometric age span (Fig. 2c). This consistency indicates that the YK1 stalagmite laminae-count age model is suitable for high precision paleoclimate reconstruction (Shen et al., 2013). The YK1 stalagmite was deposited over a period of 5.15 ka, from 37.14 to 42.30 ka BP, corresponding to 529–630 mm, covering the time interval of HS4 (Fig. 2c).

3.2. $\delta^{18}O$

The YK1 $\delta^{18}O$ values range from −9.4 to −6.2‰ (Table S3), with an average of −8.3‰, with a mean temporal resolution of 11 years. The YK1 $\delta^{18}O$ record exhibits low amplitude (~0.8‰) fluctuations during 40.75–40.21 ka BP. At 40.21 ka BP, a significant negative abrupt change occurs with an amplitude of 1.0‰ (Fig. 3a). During the period between 40.18 and 39.24 ka BP, YK1 $\delta^{18}O$ exhibited a significant and persistent positive shift, with an amplitude of 3.0‰ over 0.93 ka, and remained relatively positive overall during

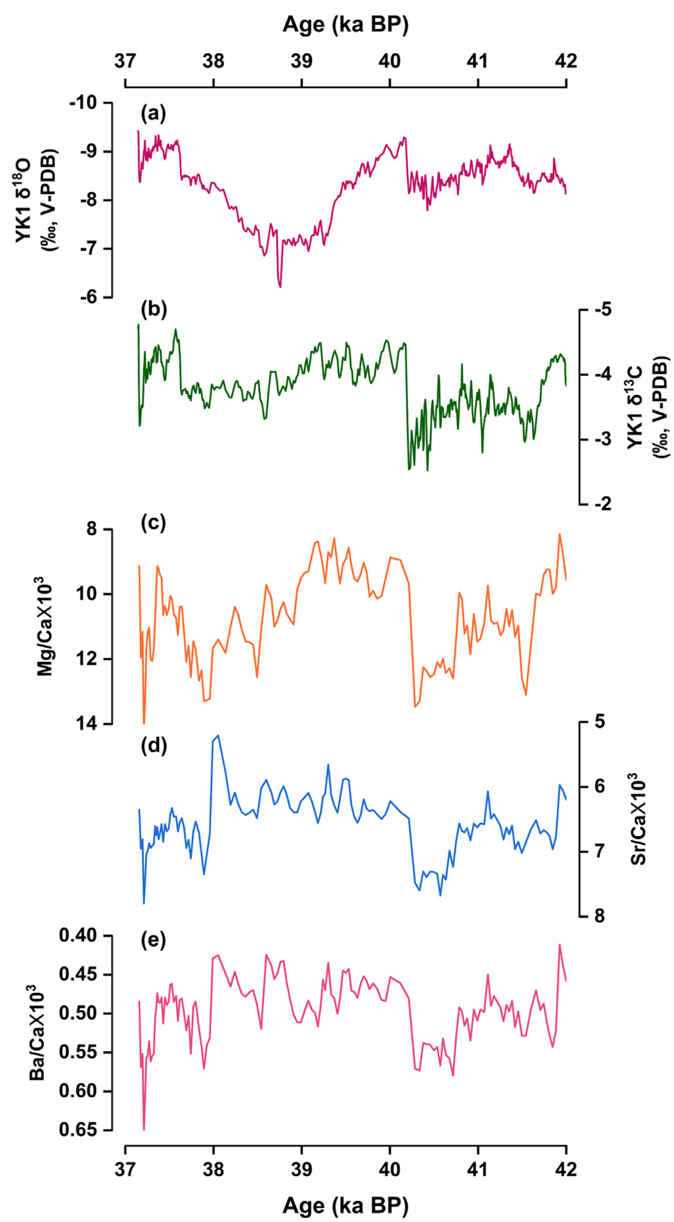

Fig. 3. $\delta^{18}O$, $\delta^{13}C$ and X/Ca records of YK1 stalagmite. **(a)** $\delta^{18}O$ record of YK1; **(b)** $\delta^{13}C$ record of YK1; **(c)** Mg/Ca record of YK1; **(d)** Sr/Ca record of YK1; **(e)** Ba/Ca record of YK1.

39.24–38.35 ka BP. During 38.35–37.14 ka BP, $\delta^{18}O$ values exhibit negative fluctuations and return to the level observed prior to the occurrence of the abrupt change at 40.18 ka BP, within 1.2 ka (Fig. 3a).

3.3. $\delta^{13}C$ and trace elements

The YK1 $\delta^{13}C$ values range from −4.7 to −2.5‰ (Table S3; Fig. 3b), with an average of −3.7‰. In contrast to $\delta^{18}O$, the variation in $\delta^{13}C$ can be divided into two parts, with the first phase at 42.00–40.21 ka BP, where $\delta^{13}C$ is rapidly positive by ~1.2‰ (0.3 ka) at 41.93 ka BP and maintains a ~1‰ oscillation for ~1.40 ka after that (Fig. 3b). The average of $\delta^{13}C$ at this stage is −3.56‰. The second phase is 40.21–37.14 ka BP. At 40.21 ka BP, similar to $\delta^{18}O$, $\delta^{13}C$ presents ~2‰ negative fluctuation, but during 40.18–39.24 ka BP, $\delta^{13}C$ does not show significant and consistent positive shifts but rather frequent fluctuations of ~0.6‰ (Fig. 3b). Although $\delta^{13}C$ only starts to be a slowly positive shift at 40.19 ka BP, the magnitude is significantly less than with $\delta^{18}O$ (3.0‰).

YK1 stalagmites Mg/Ca, Sr/Ca, and Ba/Ca exhibit significant oscillatory variation on the centennial-scales (Fig. 3c–e) (Table S4). However, after the positive abrupt shift in the X/Ca record at ~40.18 ka BP, similar to $\delta^{13}C$, the X/Ca values remain at a low level of variation, with the exception of the Mg/Ca record, where a more pronounced positive shift can be clearly identified, it is not evident in Sr/Ca and Ba/Ca (Fig. 3c–e).

The results of the correlation statistics revealed robust positive correlations between $\delta^{13}C$, Sr/Ca, Ba/Ca, and Mg/Ca ($0.24 < r < 0.89$, $p<0.01$) (Figure S3). Similar positive correlations were not observed between $\delta^{18}O$ and $\delta^{13}C$, Sr/Ca, Ba/Ca, and Mg/Ca (Figure S3). The results of the principal component analysis of the X/Ca records indicate that three principal components (PC1, PC2, PC3) explained approximately 83.7%, 12.8% and 3.5% of the total variance, respectively (Table S5). Our comparison indicates a more similar variation between $\delta^{13}C$, Sr/Ca, Ba/Ca, and Mg/Ca.

4. Discussion

4.1. Environmental interpretation of stalagmite proxies

4.1.1. $\delta^{18}O$

Modern atmospheric observations and simulations suggest that the variability of $\delta^{18}O_p$ in ASM is primarily dominated by large-scales atmospheric dynamics, with limited influence from regional precipitation (Cai et al., 2018; Li, 2018; Ruan et al., 2019; Zhang et al., 2020). On seasonal-interannual time scales, ASM $\delta^{18}O_p$ usually does not reflect local precipitation variability (Cai et al., 2018; Ruan et al., 2019; Liu et al., 2020; He et al., 2021a). However, it is affected by atmospheric convective activity in moisture sources and isotopic fractionation during transport (rainfall effect) (Liu et al., 2014; Cai et al., 2018; Li, 2018; Ruan et al., 2019; He et al., 2021b). More negative $\delta^{18}O_p$ values could be the result of enhanced convective activity in moisture source, increased precipitation in upstream areas, the seasonal movement of subtropical westerlies, and enhanced ASM circulation, but not necessarily increased precipitation in local areas (Cai et al., 2018; Li, 2018; Ruan et al., 2019; Zhang et al., 2020). Long-term cave monitoring, including Yangkou cave, has also demonstrated that $\delta^{18}O$ variations in cave drips on seasonal-interannual scales can reflect variations in $\delta^{18}O_p$ caused by large-scales atmospheric circulation (e.g., El Niño Southern Oscillation (ENSO)) (Duan et al., 2016b; Chen and Li, 2018; Zhang and Li, 2019; Qiu et al., 2021).

Although there is controversy in interpreting stalagmite $\delta^{18}O$, the perspective that stalagmite $\delta^{18}O$ is related to changes in the intensity and position of the ASM circulation is well accepted (Cheng et al., 2021; Zhang et al., 2021b; Liang et al., 2022). It is consistent with modern instrumental data, paleoclimate reconstructions, and simulation results on different time scales (Duan et al., 2016b; Chiang et al., 2020; Cheng et al., 2021; Zhang et al., 2021b). Furthermore, the consistency of the amplitudes and trends of YK1 $\delta^{18}O$ with other stalagmite records from the Asian monsoon region on the millennial-centennial scales is the evidence that the kinetic effect on YK1 $\delta^{18}O$ is negligible and that $\delta^{18}O$ reflects the signals of large-scales climate change (Dorale and Liu, 2009) (Fig. 4). The YK1 stalagmite $\delta^{18}O$ is indicative of the variations in ASM intensity and the negative shift in stalagmite $\delta^{18}O$ corresponds to an intensified ASM.

4.1.2. $\delta^{13}C$ and trace elements

The current research suggests that the variations of stalagmite $\delta^{13}C$ is related to the changes in local temperature and hydrological conditions (Spötl et al., 2005; Fairchild et al., 2006; Li et al., 2018; Fohlmeister et al., 2020; Chen et al., 2021a, 2021b). Stalagmite $\delta^{13}C$ primarily reflects regional hydrological conditions and their influence on changes in surface vegetation type and density (Dorale et al., 1998), soil biological activity (Fohlmeister et al., 2020; Jia et al., 2022). The main influences are both bio-organic processes closely related to precipitation and inorganic processes such as PCP (Hendy, 1971; Spötl et al., 2005; Fairchild et al., 2006; Li et al., 2018). Regional hydrological conditions controlled by temperature and precipitation profoundly impact surface vegetation types, soil microbial activity and CO_2 production, and cave drips inherit this environmental variation information (Cosford et al., 2009; Fohlmeister et al., 2020; Chen et al., 2021a, 2021b). The inorganic stalagmite carbon isotope transport processes have also been extensively discussed, covering cave ventilation, $_pCO_2$, stalagmite growth rates, and cave drip rates (Hendy, 1971; Fairchild et al., 2006).

Trace element contents and their ratios in stalagmites are controlled on different time scales by climatic/environmental as well as non-climatic/environmental factors (Fairchild and Treble, 2009; Warken et al., 2019; Wassenburg et al., 2020), which makes it more difficult to interpret the climatic significance of trace elements from a regional perspective. For example, these processes significantly control the distribution coefficients of Mg or Sr in calcite: temperature (Huang and Fairchild, 2001), growth rate (Gabitov et al., 2014), PCP (Fairchild et al., 2006), water-rock interaction (WRI) (Fairchild et al., 2009), soil clays (Peckover et al., 2019), etc.

Temperature can significantly affect the partition coefficient of Mg (Huang and Fairchild, 2001). A variation in temperature of 2–3 °C resulted in a maximum variation of 15% in Mg concentration (Huang and Fairchild, 2001), however, the variability of YK1 Mg/Ca varied by more than 50% before and after HS4 (Fig. 3). Even during the Last Glacial Maximum (LGM), the annual mean temperature in the low latitudes of southern China only decreased by about 4–6 °C (Xue et al., 2015). Cave monitoring for Yangkou Cave indicates that the temperature inside the cave is relatively stable (7.5 °C) and consistent with the average annual temperature of the external environment (8.5 °C) (Chen and Li, 2018). Thus, temperature changes cannot fully explain the variation in Mg/Ca. Furthermore, the growth rate of YK1 remained stable over the study period (19.6 μm/a), well below the threshold at which the growth rate affects Sr and Mg (315 μm/a) (Gabitov et al., 2014). Temperature and growth rate may not be the main factors influencing trace element variation in this study.

Trace element concentrations in cave drips are associated with the rock mineral composition of the overlying bedrock of the cave (Chen and Li, 2018; Li et al., 2021b). For example, karst water transport through dolomite or limestone can result in the

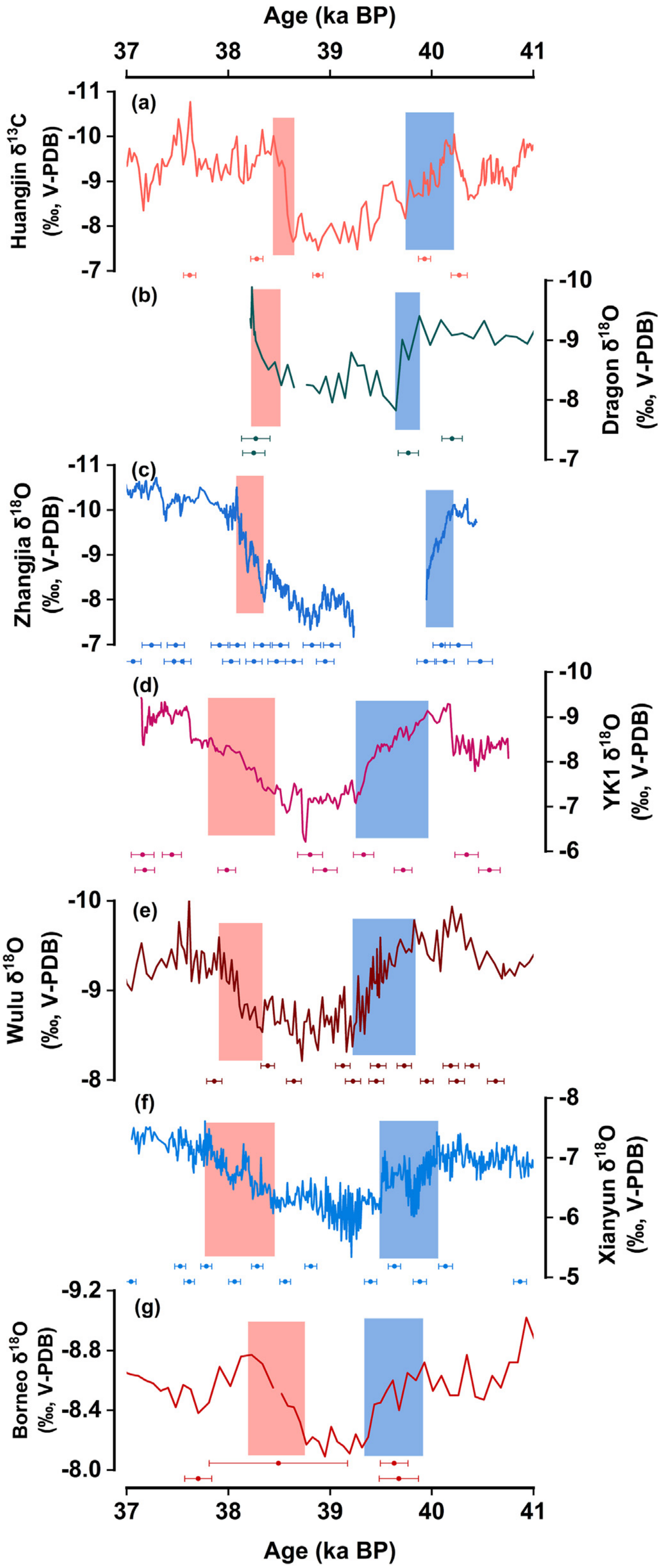

Fig. 4. The HS4 YK1 $\delta^{18}O$ record compared with climatic records for the Asian monsoon region. **(a)** stalagmite $\delta^{13}C$ record from Huangjin cave (Liang et al., 2022); **(b)** stalagmite $\delta^{18}O$ record from Dragon cave (Dong et al., 2018); **(c)** stalagmite $\delta^{18}O$ record from Zhangjia cave (Cheng et al., 2021); **(d)** YK1 $\delta^{18}O$ record (This study); **(e)** stalagmite $\delta^{18}O$ record from Wulu cave (Liu et al., 2018; Cheng et al., 2021); **(f)** stalagmite $\delta^{18}O$ record from Xianyun cave (Zhang et al., 2021d); **(g)** stalagmite $\delta^{18}O$ record from Borneo cave (Carolin et al., 2013). The blue/red boxes correspond to the onset/termination of HS4. Order of records from top to bottom by latitude. (For interpretation of the references to colour in this figure legend, the reader is referred to the Web version of this article.)

differential dissolution of Mg^{2+} or Sr^{2+} in cave drips (Fairchild and Treble, 2009; Tremaine and Froelich, 2013; Warken et al., 2019). If the transport pathway of infiltration water is changed, it will alter the initial signal of trace element ratios that are unaffected by environmental changes, which in turn will mislead the interpretation of stalagmite X/Ca climate and environmental signals (Fairchild and Treble, 2009; Tremaine and Froelich, 2013; Warken et al., 2019). Sr/Ca and Mg/Ca in cave drips and speleothems as wet/dry proxies (PCP) require that Mg/Sr remain stable, i.e., the cave drip transport pathway is not changing (the mixing ratio of different types of bedrock remains constant) (Tremaine and Froelich, 2013). Yangkou cave developed in the predominantly medium and thick-bedded massive bioclastic limestone, with no significant variation in the composition of host rock. In addition, calculations of Mg/Sr for YK1 stalagmites showed a mean Mg/Sr value of 1.75 and a standard deviation of 0.17. Variations of X/Ca in the stalagmite YK1 inherit and preserve the signals of external climatic and environmental change.

As the distribution coefficients of trace elements are usually less than 1 and much less than Ca, the PCP indirectly reflects climate and environmental changes by controlling the ratio of trace elements to Ca in the cave drips (Fairchild and Treble, 2009). The enhancement of PCP leads to much greater reduction in Ca than trace elements during calcite precipitation, implying an increase in the ratio of trace elements such as Mg and Sr to Ca in cave drips and speleothem (Cruz et al., 2007; Fairchild and Treble, 2009; Zhang et al., 2018). Longer WRI times result in more trace elements in the bedrock being dissolved into the drip water, and saturation of these elements leads to an increase in the X/Ca (Fairchild et al., 2009). The impacts of PCP and WRI on trace element ratios is in the same direction. Under the influence of these mechanisms, variations in the mean state of the dry-wet transition (water balance) of the regional environment control the variation of trace element ratios in stalagmites through PCP/WRI processes (Fairchild et al., 2006; Fairchild and Treble, 2009; Wassenburg et al., 2020).

PCP can significantly influence the $\delta^{13}C$ of cave drips and speleothem (Stoll et al., 2015; Fohlmeister et al., 2020). When cave drips are transported or degassed for longer times during deposition, $\delta^{13}C$ tends to be positive (Fohlmeister et al., 2020; Lechleitner et al., 2020). Our records show that $\delta^{13}C$ and X/Ca have similar trends across time and exhibit significant positive correlations ($0.24 < r < 0.52$, $p < 0.01$) (Figure S3). Variations in speleothem $\delta^{13}C$ and X/Ca are usually controlled by regional environment, such as precipitation, infiltration processes of water in the epikarst, etc. (Li et al., 2018; Fohlmeister et al., 2020; Xue et al., 2021; Jia et al., 2022). Our previous research has also demonstrated that $\delta^{13}C$ is largely controlled by hydroclimatic processes, whether on the orbit-millennial or centennial scales (Wu et al., 2020). $\delta^{13}C$ can verify the plausibility of our interpretation of the climatic significance of trace elements, and it is valid and reasonable to explore regional hydroclimatic variability through the combination of multiple indicators (Chen et al., 2021a, 2021b).

In summary, we have ruled out the influence of non-climatic factors on stalagmite X/Ca where possible. PCP and WRI influenced by regional precipitation and hydrological conditions may be the dominant factors in X/Ca variation. On the centennial-millennial scales, monsoonal precipitation controls the variability of $\delta^{13}C$ and X/Ca by influencing the mean state of the effective soil moisture balance. Decreased regional precipitation and deteriorated hydrological conditions lead to reduced vegetation cover and soil microbial activity, weaker soil CO_2 productivity, lower effective moisture and increased PCP, which result in positive $\delta^{13}C$ and increased X/Ca in cave drips and stalagmite (Chen and Li, 2018; Li et al., 2018; Chen et al., 2021a, 2021b). The decoupling of $\delta^{18}O$ with $\delta^{13}C$ and X/Ca indicates that variations in the regional hydrological environment during HS4 may be controlled by factors other than ASM intensity.

4.2. ASM variation during HS4 in monsoonal China

The ASM intensity recorded in stalagmite $\delta^{18}O$ from different regions of the ASM is characterized by significant positive shift at ~40.00 ka BP, with an average magnitude close to 2.0‰, indicating that the ASM intensity was rapidly weakened at this time under the influence of North Atlantic climate change (Fig. 4) (Dong et al., 2018; Cheng et al., 2021; Zhang et al., 2021d; Liang et al., 2022). Although there are differences in the resolution of these stalagmite $\delta^{18}O$ records, the ASM intensity within HS4 does not exhibit a stable weak monsoon condition but there is significant oscillation on the centennial scales. For example, the Zhangjia $\delta^{18}O$ record exhibits negative fluctuations of ~1.1‰ between 39.23 and 38.95 ka BP, followed by a positive shift of ~0.9‰ (Fig. 4c), while the YK1 $\delta^{18}O$ shows two large positive fluctuations at 38.78 and 38.64 ka BP (Fig. 4d). The comparisons suggest that the internal structure of the ASM is unstable during HS4.

The response process of stalagmite $\delta^{18}O$ in HS4 is not consistent in the southern and northern monsoon regions of China (Dong et al., 2018; Liu et al., 2018; Cheng et al., 2021; Liang et al., 2022; Zhang et al., 2021d) (Fig. 4). The stalagmite records of northern China are characterized by the rapid transition at the onset and termination of HS4 (Fig. 4a–c) (Figures S4 and S5). In northern China, for example, the onset of HS4 lasted for 0.23 (Dragon cave) (Figs. 4b) and 0.47 ka (Huangjin cave) (Fig. 4a), and the termination of HS4 is similarly fast, only 0.29 and 0.26 ka, respectively. Although the stalagmite from Zhangjia cave exhibits a depositional hiatus at 38.95 ka BP, it also exhibits a rapid positive shift in $\delta^{18}O$ at the onset of HS4 (~2‰ within 0.25 ka) (Fig. 4c). In contrast, in southern China, the onset of HS4 in the $\delta^{18}O$ records from the Indian summer monsoon (ISM) affected Yangkou cave and Wulu cave is as long as 0.89 and 1.02 ka, with the termination of HS4 lasting 0.57 and 0.40 ka (Fig. 4d–e). The onset (0.50 ka) and termination (0.72 ka) of HS4 in the EASM influenced Xianyun $\delta^{18}O$ record are similarly longer than in northern China (Zhang et al., 2021d) (Fig. 4f). The Bayesian change point analysis results also indicate that the abrupt change characteristics of the stalagmite records in northern China are more significant in the overall event (Ruggieri, 2013) (Figure S4). The ASM intensity in southern China has experienced several large-amplitude fluctuations during the transition but remains in a gradual variation process overall (Fig. 4).

4.3. Differences in climate change processes at NH high - low latitudes during HS4

The rapid shifts in the northern China stalagmite records during the onset/termination of HS4 are consistent with variations in North Greenland Eemian deep ice core (NEEM) $\delta^{18}O$, North Greenland Ice Core Project (NGRIP) *d*-excess and dust concentrations (Fig. 5a–c and S5). NEEM $\delta^{18}O$ rapidly responded to the HS4 onset (0.24 ka)/termination (0.06 ka) transitions (Fig. 5a and S5). The NGRIP *d*-excess associated with the HS4 onset (0.25 ka)/termination (0.19 ka) also responded rapidly (Fig. 5b). At the same time, NGRIP dust concentrations increased rapidly (0.20 ka), as well as decreased (0.17 ka) (Fig. 5c). Paleoclimate records from the high latitudes of the NH show that the proportion of onset and termination processes of HS4 account for about 20% of the overall event, while it exceeds 50% at lower latitudes (Table S1).

The stalagmite $\delta^{18}O$ records in southern China exhibit a gradual transition process at the onset/termination of HS4 consistent with the paleoclimatic records from low latitudes and the SH (Fig. 4d–g and 5e-g, i-k) (Figure S5). The NEEM ^{17}O-excess, for example, which reflects the variation of hydrological cycle strength at low latitudes, remained high (~55 permeg) (Fig. 5e) (Guillevic et al., 2014). Although the SAM started to strengthen at ~40.05 ka BP accompanied by increasing summer precipitation, the relatively positive stalagmite $\delta^{18}O$ values (~-3.0‰) at this time indicate that SAM did not reach the strongest state of HS4 (Fig. 5h). The YK1 $\delta^{18}O$ and the total reflectance records of Arabian Sea sediment core indicate that the ITCZ in this area was experiencing a slow southward shift with a gradual weakening ASM intensity (Fig. 5i) (Deplazes et al., 2013). The Antarctic experienced gradual warming under the influence of the 'thermal bipolar seesaw' and enhanced deep-sea convection in the Southern Ocean (Fig. 5i–k) (WAIS Divide Project Members, 2015; Skinner et al., 2020). It is evidenced that the climate responses at low latitude and SH to HS4 are not completed sharply but with a gradual trend experienced several large fluctuations (Fig. 5, S4, and S5).

With stable Greenland temperatures, the West Antarctic Ice Sheet (WAIS) ice core $\delta^{18}O$ and the South Ocean deep-water temperature indicated that the Antarctic temperature/Southern Ocean deep convection had started to decrease/weaken slowly around 38.80 ka BP (Skinner et al., 2020) (Fig. 5j–k). Atmospheric CO_2 also increased rapidly by ~16 ppm at 39.64 ka BP (Fig. 5j). Low-latitude paleoclimate records start to shift successively towards GI 8 during 39.00–38.50 ka BP (Fig. 5e–j). However, the abrupt Greenland temperature rise and AMOC recovery lagged the transition from HS4 to GI 8 at low latitudes (~38.34 ka BP) (Fig. 5a–c) (Landais et al., 2018; Gkinis et al., 2021), plausibly indicating that the termination of HS4 occurred first at low latitudes and SH followed with more gradual process.

4.4. Climate driven mechanisms

The collapse of the Laurentide ice sheet and the influx of freshwater into the North Atlantic caused abrupt weakening or collapse of AMOC (Fig. 5d) (Bassis et al., 2017; Ziemen et al., 2019). The temperature in Greenland is susceptible to changes in the sea ice in North Atlantic. With the expansion of sea ice, the temperature in the Greenland decreased and HS4 onset occurred rapidly at ~40.10 ka BP (Fig. 5a–b) (Guillevic et al., 2014; Landais et al., 2018; Gkinis et al., 2021). Intense cooling air at high latitudes in NH can lead to increase the meridional temperature gradient between the high and low latitudes, and strengthen southward shift of the NH westerlies (Fig. 5c) (Duan et al., 2016a; Liang et al., 2022). This process propagated abrupt climate change signals in the North Atlantic rapidly to the East Asian monsoon regions through atmospheric circulation.

In contrast to the "sawtooth" structure of the Greenland ice core and the paleoclimate record of northern China, the "gradual" pattern of the low latitude and SH paleoclimate records indicates different climate forcing mechanisms between them.

At the onset of HS4, a longer adjustment interval is needed for the transition of climate change in the low latitudes responding to HS4 via the interaction between ocean-atmosphere systems, because of the gradual modulation of heat storage in the tropical oceans (Stocker and Johnsen, 2003; Pedro et al., 2018). The interhemispheric thermal gradient, particularly the north-south equator thermal gradient, is the driving force for the shifts of ITCZ (McGee et al., 2014, 2018; Burns et al., 2022). The process of cooling of the tropical oceans and changes in the interhemispheric/north-south equatorial temperature gradient are not as dramatic as the temperature variations in the NH high latitude (Pedro et al., 2018;

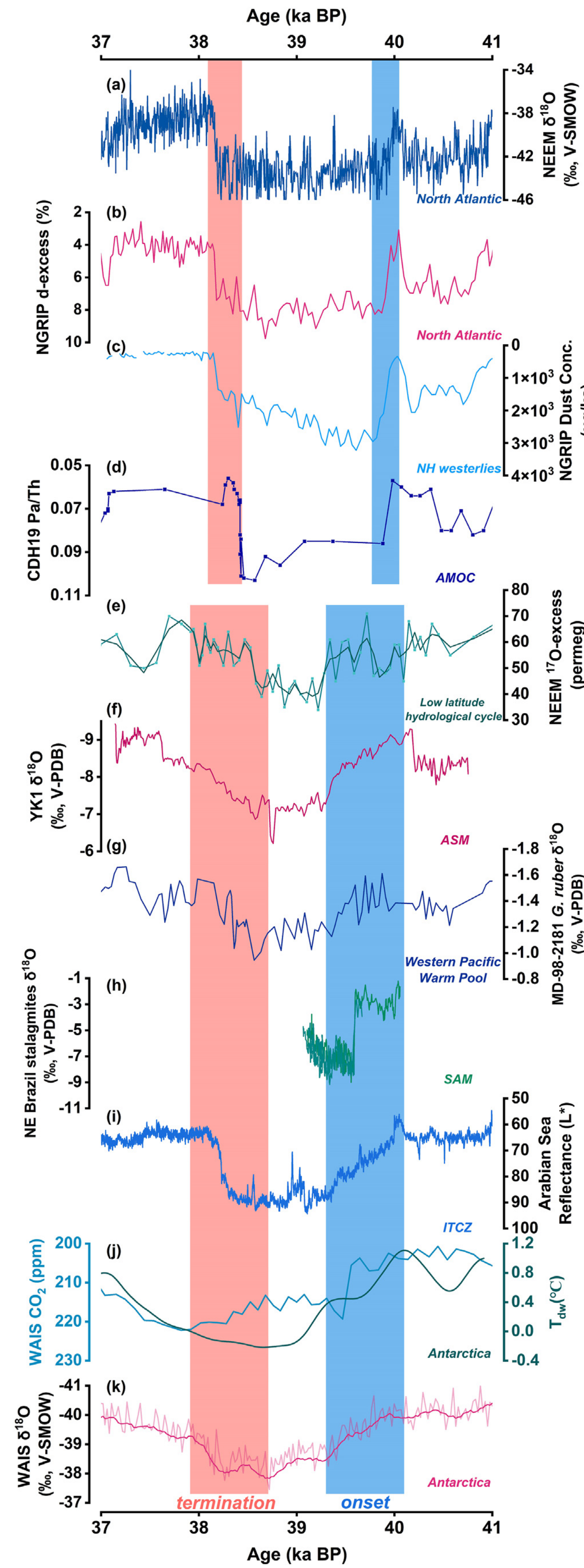

Skinner et al., 2020), resulting in the gradual southward shift of the ITCZ during HS4 onset (Guillevic et al., 2014). Low-latitude hydroclimate indicator (^{17}O-excess) on the same chronology as the NEEM δ^{18}O have demonstrated that the southward shift of the ITCZ during HS4 onset lagged the onset of Greenland cooling by ~550 ± 60a and that the process is much more gradual (Fig. 5e) (Guillevic et al., 2014). The simulations also confirm that the intensity of air convection and atmospheric circulation in WPWP are the major factors controlling the variability of precipitation δ^{18}O in ASM (Cai et al., 2018; Ruan et al., 2019). The decreasing continental-oceanic thermal gradient and the intensity of tropical atmospheric convection during HS4 also tends to weaken the ASM and result the positive shift of $\delta^{18}O_p$ (Wang et al., 2017; Ruan et al., 2019; He et al., 2021a), this process is also more gradually. At the same time, precipitation in northeastern Brazil, although beginning to increase at 40.05 ka (Fig. 5h), appeared to increase dramatically at ~39.60 ka, indicating an abrupt southward shift of the ITCZ compared to the previous phase (Wendt et al., 2019), which may be related to the difference of ITCZ movement amplitude and contraction/expansion in different regions (McGee et al., 2014, 2018; Yan et al., 2015).

During HS4, the collapse or weakening of the AMOC leads to significant heat accumulation in the tropical Ocean and Southern Ocean, which eventually triggers the termination of HS4 (Stocker and Johnsen, 2003; Pedro et al., 2018; Skinner et al., 2020). Enhanced convection in deep Southern Ocean increased the loss rate of heat and CO_2 from both the intermediate and deep oceans (Fig. 5). This eventually initiated glacial thawing at SH high latitudes and temperatures rising in Antarctic (Fig. 5 j-k) (Menviel et al., 2018; Rae et al., 2018; Skinner et al., 2020). Warming in the Southern Ocean and tropical oceans will control the slowly northward shift of the ITCZ by controlling the north-south cross-equatorial temperature gradient (McGee et al., 2014, 2018; Bradley and Diaz, 2021; Burns et al., 2022; Qiu et al., 2022). For example, the significant decrease in precipitation in northeastern Brazil at 39.10 ka BP and the start of the positive shift of the NEEM ^{17}O-excess at 38.64 ka BP indicate that the ITCZ has started to move northwards (Fig. 5e, h) (Guillevic et al., 2014; Wendt et al., 2019). The cooling of the Antarctic will gradually increase the intensity of the transport of moisture and potential heat from the Southern Indian Ocean to the ASM region via the Mascarene High and the Somali jet, contributing to the gradual intensification of the ASM in the middle to late HS4 (Nair et al., 2019; Wu et al., 2020). The increase of SST in the WPWP also contributes to the enhanced convection of atmosphere and moisture over the ocean, transporting more moisture to the ASM region through the progressively increasing sea-land thermal gradient (Wang et al., 2017). The stalagmite in South American stopped growing at ~39.10 ka BP (Fig. 5h), indicating that the ITCZ in South America had moved northwards at this time, and SAM precipitation decreased (Wendt et al., 2019; Cheng et al., 2021). Recent research has highlighted the important role of reduced Amazon River runoff and associated sea surface salinity

Fig. 5. Decoupling variations between paleoclimate records in different regions during HS4. **(a)** NEEM ice core δ^{18}O record (Gkinis et al., 2021); **(b)** NGRIP ice core *d*-excess record (Landais et al., 2018); **(c)** NGRIP dust concentration record (Urs et al., 2007); **(d)** Bermuda Rise CDH19 Pa/Th record (Henry et al., 2016); **(e)** NEEM ice core ^{17}O-excess record (Guillevic et al., 2014); **(f)** YK1 stalagmite δ^{18}O record (this study); **(g)** MD-98-2181 *G. ruber* δ^{18}O records of the Western Pacific Warm Pool MD98-2181 (Saikku et al., 2009); **(h)** South America Toca da Boa Vista (TBV) and Toca da Barriguda (TBR) cave δ^{18}O records (Wendt et al., 2019); **(i)** Arabian Sea SO130-289 KL sediment total reflectance (Deplazes et al., 2013); **(j)** Green curve indicates WAIS CO_2 record (Bauska et al., 2021), the blue curve indicates Southern Ocean deep-water temperature record (Skinner et al., 2020); **(k)** WAIS Divide ice core δ^{18}O record (Buizert et al., 2018). The blue/red boxes correspond to the onset/termination of HS4. (For interpretation of the references to colour in this figure legend, the reader is referred to the Web version of this article.)

anomalies in the termination of HS4 and HS2 (Cheng et al., 2021; Dong et al., 2022). In the tropical Atlantic, sea surface salinity in the Amazon Plume Region increases because of reduced precipitation and runoff in the Amazon Basin and is subsequently increased northward salt transport by shallow AMOC or an overturning circulation involving the North Atlantic Intermediate Water (Liang et al., 2020; Cheng et al., 2021). This process provides positive feedback for the recovery of the AMOC (Waelbroeck et al., 2018; Skinner et al., 2020), ultimately promoting the northward shift of ITCZ, strengthening the ASM, and the termination of HS4 (Cheng et al., 2021). The factors mentioned above have profound implications for the variations in ASM, including moisture sources, precipitation and $\delta^{18}O_p$, so that the termination of HS4 is first observed in the monsoon/hydrological records at low latitudes and SH (Fig. 5 and S5). In contrast, as the North Atlantic was covered by sea ice, heat accumulated below the halocline until reaching certain threshold which disrupted stable stratification within the ocean and triggered vertical convection. Simultaneously, warm water quickly reached the surface ocean and sea ice was rapidly melted, leading to sudden warming in Greenland (Fig. 5) (Bradley and Diaz, 2021; Li and Born, 2019).

Tropical hydroclimatic anomalies, such as super ENSO in tropical oceans, regulate the gradual transition of climate in the WPWP and southern China. Higher salinity and lower than normal SST in WPWP during stadials correspond to El Niño (Stott et al., 2002). ENSO and the tropical Pacific SST regulate precipitation and atmospheric circulation anomalies in the ASM (Merkel et al., 2010; Cai et al., 2017; Liu et al., 2019a, b; Jiang et al., 2021). In the El Niño-like state, the weakening Walker circulation over the eastern and western Pacific led to prevailing anticyclonic motion and subsidence in the western tropical Pacific (Yu et al., 2015; Yang et al., 2017), which ultimately resulted in the strengthening and westward movement of WPSH and weakening the EASM (Jiang et al., 2021; Wang et al., 2022a, b). Tropical hydroclimatic processes such as the equatorial east-west Pacific SST and variations in interhemispheric temperature gradient require longer response and adjustment times to abrupt climate events than AMOC and sea ice, with the result that the response of the tropics to climate changes in high-latitude climate may be considerably smoother (Stott et al., 2002; Deplazes et al., 2013). Recent research has pointed out that the gradual transition presented by ASM during the onset and termination of HS4 was consistent with the variation of SST in the tropical western Pacific (Zhang et al., 2021d). The gradual processes observed in our records emphasized that tropical hydrological and the ENSO leading to the gradual transition of the ASM by controlling WPSH and EASM intensity.

In summary, our record provides robust evidence that the tropical ocean controls the gradual onset and first termination of HS4 at low latitudes through oceanic (sea-land thermal and interhemispheric temperature gradients) and atmospheric processes (ITCZ). We also highlight the teleconnections between temperature changes in the SH and ASM dynamics via ocean-atmosphere interconnection.

4.5. Decoupling between ASM and regional hydrological environment during HS4

During Greenland Stadials (GS) 10, YK1 $\delta^{18}O$ shows a positive shift of ~1‰, indicating that the ASM intensity is weakened (Fig. 6a). The $\delta^{13}C$ and X/Ca PC1 records also display positive shifts of ~1.2‰ and ~3.4 (Fig. 6b–c), associated with reduced precipitation, degraded ecology, weakened biological activity and reduced biologic-CO_2 production overlying Yangkou cave under the influence of weakened ASM and southward shift of the ITCZ. As the ASM transition from GS10 to GI9, $\delta^{13}C$ and X/Ca PC1 exhibit a negative

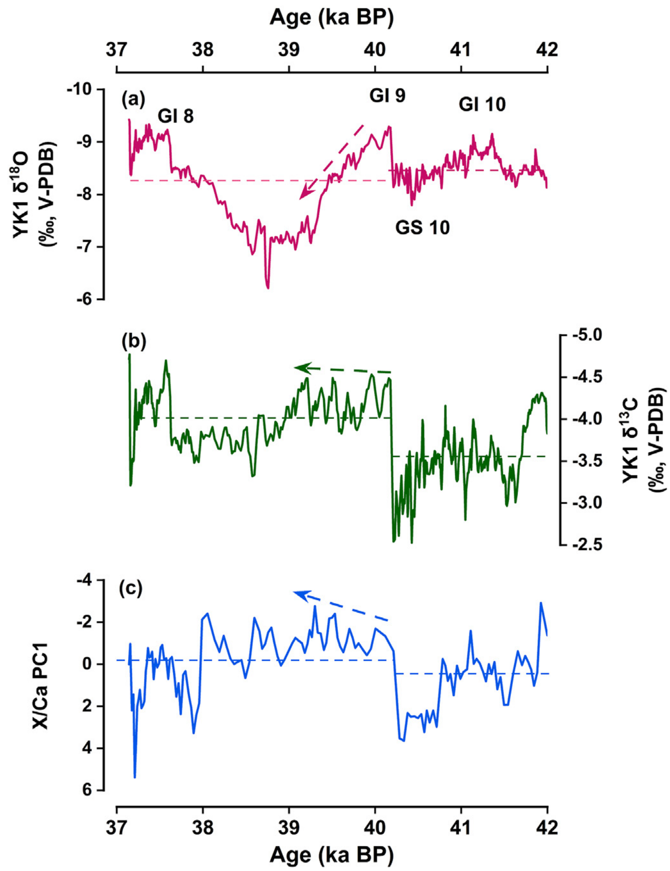

Fig. 6. $\delta^{18}O$, $\delta^{13}C$ and X/Ca PC1 records of YK1 stalagmite. **(a)** $\delta^{18}O$ record of YK1; **(b)** $\delta^{13}C$ record of YK1; **(c)** X/Ca PC1 records of YK1. Dashed lines indicate the mean values recorded at different stages (37.14–40.21 ka BP, 40.21–42.00 ka BP). GI and GS indicate Greenland Interstadials and Greenland Stadials.

shift, indicating an improvement in vegetation and hydrological environmental conditions (Fig. 6). The strong covariation characteristics of the different climatic indicators ($\delta^{18}O$, $\delta^{13}C$, X/Ca) in YK1 stalagmites during 40.25–42.00 ka BP indicate that the variation of ASM intensity is an important factor to control stalagmite $\delta^{13}C$ and X/Ca values by influencing regional hydrological conditions and ecological environments (Fig. 6 and S6) (Li et al., 2018; Chen et al., 2021a, 2021b).

The obvious weak ASM observed in $\delta^{18}O$ (overall variability ~3‰) is not evident in $\delta^{13}C$ and X/Ca PC1 (Fig. 6). During 40.17–39.25 ka BP, the ASM gradually weaken and the $\delta^{13}C$ and X/Ca PC1 do not show obvious trends of positive shifts, but rather frequent fluctuations in maintaining the level of GI9 (Fig. 6), indicating that the regional environment is not significantly degraded at this time. However, we also observed a small positive shift in $\delta^{13}C$ and X/Ca PC1 during 39.18–38.73 ka BP ($\delta^{13}C$–0.7‰, X/Ca PC1 ~ 2.72), which remained relatively positive for about 1.00 ka thereafter and suddenly became negative at 37.65 ka BP in synchrony with the $\delta^{18}O$ into GI8 (Fig. 6). The variations of $\delta^{13}C$ and X/Ca PC1 within HS4 are divided into two phases, frequent oscillations on the centennial scales based on an overall negative in the early phase, and a small positive shift in the later phase (Fig. 6). But even if these records are positive in the later phase, the mean values remain significantly lower throughout HS4 than GS10, and the magnitude of variations in these records in the later phase is much smaller than that during the GI9-S10-GI9 transition.

We performed a lead-lag analysis of $\delta^{18}O$ with $\delta^{13}C$ and X/Ca PC1 records. The results indicated that there is no significant lead-lag relationship between $\delta^{18}O$-$\delta^{13}C$ and $\delta^{18}O$-X/Ca PC1 (Figure S7). X/Ca PC1 only lags $\delta^{18}O$ by about 0.05 ka, which may be explained by the lower resolution of X/Ca PC1, and 0.05 ka is far less than the time scales we discussed. It is also evident from visual inspection that these records occur almost simultaneously during the rapid transition between GS10-GI9 and HS4-GI8 (Fig. 6), indicating that all three are able to respond rapidly to variations in the external climate and environment. We therefore consider that there is no systematic lead-lag relationship between $\delta^{18}O$ and $\delta^{13}C$ or X/Ca PC1. The small positive shift in $\delta^{13}C$ and X/Ca PC1 in the late HS4 is part of the internal fluctuation of the regional environment during HS4, that is, the late HS4 is slightly drier relative to the early, but the regional wet-dry balance conditions are better than GI10 and GS10.

The inconsistency of X/Ca PC1 and $\delta^{13}C$ with $\delta^{18}O$ during HS4 suggests that the ASM is decoupled from regional precipitation and environmental variations. It presents a moderate hydrological environment with no significant ecological deterioration. This situation is linked to 2 factors: (1) During HS4, although ASM decreased significantly, the PCP level of the cave system remained approximately at GS10 because there was no significant decrease in regional precipitation or effective humidity. (2) Despite the decreasing of annual mean surface temperature in the NH, the vegetation was dominated by C3 and evaporation was probably weakened by the lower temperatures. The regional hydrological environment, vegetation density and soil biological activity might not deteriorate significantly, resulting in no significant decrease in soil CO_2 production (Wu et al., 2020). Finally, $\delta^{13}C$ of stalagmite did not show significant positive shift similar to that of $\delta^{18}O$.

Although ASM is weakened during HS4, the positive shift of YK1 $\delta^{18}O$ does not necessarily indicate decrease in regional precipitation. The variation of $\delta^{18}O_p$ in the EASM region is mainly influenced by the convective activities of the moisture source, the atmospheric circulation patterns and the upstream amount effect, while the regional precipitation has a limited effect (Li, 2018; Ruan et al., 2019). The moderate environments indicated by YK1 $\delta^{13}C$ and X/Ca are associated with changes in EASM rainfall bands movement (Ding et al., 2018; Zhang et al., 2021b). A series of observations and simulation research have indicated that the duration of EASM precipitation and the seasonal variation of circulation are strongly related to the seasonal north-south movement of the subtropical westerlies across the Tibetan Plateau (Chiang et al., 2020; Zhao et al., 2021a), which results in the different spatial variability of precipitation in the EASM area. The timing and strength of the northward shift of the subtropical westerlies affect the phase variation and duration of spring, pre-Meiyu, Meiyu and summer precipitation in southern China (Ding et al., 2018; Chiang et al., 2020; Zhang et al., 2021b). An earlier transition of the subtropical westerlies to the northern Tibetan Plateau will push the summer rainfall bands to the north earlier, which result in a significant shorter Meiyu season and longer summer. Finally, tripole pattern is formed with lower precipitation in central China and higher precipitation in northern and southern China (Zhang et al., 2018; Herzschuh et al., 2019).

During HS4, enhanced Hadley circulation suppressed the northward shift of the subtropical westerlies due to the increased temperature gradient between high and low latitudes in the NH (McGee et al., 2018; Zhao et al., 2020, 2021a). The Hadley circulation, an overturning circulation driven by differential heating at the Earth's surface, consists of ascending branch (ITCZ) and sinking branch (subtropical westerlies) (Hartmann, 2016; Zhao et al., 2020). In the case of warmer boreal summer will increase the cross-equatorial temperature gradient, thus shifting ascending branch (ITCZ) northwards. At the same time, a decrease of the equatorial-arctic temperature gradient also weaken the Hadley circulation (McGee et al., 2018; Routson et al., 2019; Zhao et al., 2020). This eventually causes air masses uplifted from the tropics to reach further north before sinking, thus contributing to the northward shift of the subtropical westerlies (Chiang et al., 2015, 2017; Zhao et al., 2020). In contrast, during HS4, decreased north-south cross-equatorial temperature gradient because of colder boreal summer, leading to the ITCZ shifted southward (McGee et al., 2014; Burns et al., 2022). On the other hand, the increased equator-arctic temperature gradient contributes to the strengthening of the Hadley circulation and the faster sinking of air masses, which eventually leads to the southward shift of the subtropical westerlies (Chiang et al., 2017; Routson et al., 2019).

The westerlies north of the Tibetan Plateau moves later or extended to the south, resulting in prolonged spring precipitation in southern China, seasonal weakening in summer, as well as a prolonged Meiyu rainy season and increased precipitation in the Yangtze River basin in central China (Zhang et al., 2018; Chiang et al., 2020; Wang et al., 2022b). In addition, the $\delta^{18}O_p$ in spring precipitation is significantly positive compared with that in summer, coupled with the southward shift of the ITCZ and the weakening moisture convection in the tropical Indian Ocean, it could also lead to a significant positiver $\delta^{18}O_p$ in the downstream region, while the effect on regional precipitation is not remarkable (Tan, 2014; Chiang et al., 2020; Zhang et al., 2021b; Zhao et al., 2021b). In the later phase of HS4, the gradual northward shift of the ITCZ, and the gradual intensification of the ASM circulation will cause subtropical westerlies to begin to gradually move northward (Zhao et al., 2020), pushing the long-term southerly rainfall bands of early HS4 northward. As the NH high latitudes are still cold at this time, the temperature gradient between the NH high and low latitudes has not changed significantly (Gkinis et al., 2021), resulting in a limited northward push of the rainfall bands, regional environmental conditions have only degraded slightly relative to the early HS4, but are still on the humid side overall.

Several paleoclimate records from the middle and lower Yangtze River basin show relatively wet conditions in millennial-scales climatic events (YD and HS1) during the LGM and last deglaciation (Zhang et al., 2018; Liu et al., 2019a), in contrast to the recently published high-resolution multi-proxy paleoclimate records during the last glacial period by Wang et al., 2022b. This research suggests that variations in the regional environment during the last glacial period are synchronous with ASM (Wang et al., 2022b). The regional environment is dry in the stadial, while is wet in the interstadial. Our new records suggest that the regional environment is wet during HS4. The different hydroclimatic characteristics presented by these records may be related to differences in the location and intensity of rainfall bands at different boundary conditions, seasonal differences in precipitation at different cave locations, and other regional factors such as altitude.

Extensive modelling has indicated that the wet conditions in the middle and lower reaches of the Yangtze River during YD and HS1 are associated with the southward shift of the subtropical westerlies caused by the weakening of the AMOC, as well as the prolongation of the Meiyu season (Zhang et al., 2018; He et al., 2021a, 2021b). Compared to marine isotope stage (MIS) 3, the climatic boundary conditions of the last deglaciation are more complex. For example, reduced global ice volume (Lisiecki and Raymo, 2005), weakened AMOC stability (Brovkin et al., 2021), and large meltwater discharge events in the Antarctic can significantly influence spatial differences in ASM monsoon precipitation through teleconnection (Weber et al., 2014; Zhang et al., 2016). In contrast, the boundary conditions are more stable during MIS 3, and the spatial heterogeneity of the precipitation pattern may alter accordingly. Wang et al., 2022b also emphasize that the mechanisms driving spatial differences in precipitation in eastern China during the last deglaciation (subtropical westerlies and Meiyu) may not be applicable with the last glacial period and that the ITCZ may be the primary driver of precipitation variability in the Yangtze River basin during the last glacial period.

The wet condition of HS4 indicated by YK1 is not observed in HS5 and HS6 at Yongxing cave, which may be related to the location of the Meiyu rainfall bands. The modern Meiyu zone ranges from 25 to 33°N (Ding et al., 2018). Compared to Yangkou cave (29°02′N), Yongxing cave (31°35′N) is closer to the boundary of the Meiyu zone and may be more sensitive to changes in the location of the Meiyu. During HS4, due to the southward shift or prolonged location of the Meiyu in southern China (Zhang et al., 2018; Chiang et al., 2020), the Yangkou cave may better record the increased precipitation of Meiyu at this time.

In addition to spring precipitation, the autumn rains in western China may also be responsible for the potential increased precipitation in Yangkou cave area during HS4. Compared with Yongxing cave, Yangkou cave is closer to the influence area of autumn rains in westen China (Bai and Dong, 2004; Zheng et al., 2018). Our cave monitoring work also suggests that autumn precipitation in the Yangkou cave area may account for ~30% of the annual precipitation (Chen and Li, 2018). The last glacial period Greenland stadials has the potential to perpetuate the super ENSO in the tropical Pacific (Stott et al., 2002). The combination of the ENSO and Indian Ocean Dipole positive phases can enhance moisture transport by the southwest monsoon, which consequently increases the precipitation of autumn rains in western China (Xu et al., 2016). Our 6-year monitoring also indicates that during El Niño, increased near-source moisture from the western Pacific and South China Sea resulted in positive $\delta^{18}O$ in precipitation and cave drips, as well as lower drip Mg/Ca due to higher precipitation (Chen and Li, 2018). Finally, the elevation of Yangkou cave (~2140 m a.s.l) is approximately 1340 m higher than that of Yongxing cave (~800 m a.s.l). The difference in altitude also has the potential to influence climatic and environmental variation processes outside the cave.

5. Conclusions

This study provides the highest resolution stalagmite $\delta^{18}O$ record (11a) available from southwest China during HS4. The onset/termination of the ASM response to HS4 was gradual in southern China. The reasons for this characteristic is the sluggish response of the atmospheric and hydrological cycles at low latitudes to abrupt climatic changes at high northern latitudes and the influence of temperature changes in the SH on the ASM through the cross-equatorial jet. The onset of the HS4 termination in paleoclimate records from low latitudes and the Antarctic were significantly earlier than corresponding temperature changes in Greenland. The relatively wet hydrological environment maintained in Yangkou cave area during HS4 is related to the late shift of the subtropical westerlies northward, the weakening of the summer season and the increased precipitation in the Yangtze River basin in central China. Our research highlights the non-homogeneous relationship between ASM intensity and precipitation in southwest China and the essential role of the atmospheric-ocean interaction at low latitudes and the Southern Ocean in triggering abrupt climate change events on millennial-scales during the last glacial period.

Authorship contribution statement

T.-Y.L. and J.Y.L obtained funding, conducted the fieldwork, conceptualized this study and revised the manuscript. Y.W. Writing - original draft. H.C., Y.F.N., C.-C.S., Y.Y., J.Y.Z., C.-J.C., M.-Q.L., S.Y.X., H.Y.Q., Y.Z.X., Y.Y.H., J.Y.L., T.-L.Y., R.L.E., carried with sampling, ^{230}Th dating and data analysis.

Declaration of competing interest

The authors declare that they have no known competing financial interests or personal relationships that could have appeared to influence the work reported in this paper.

Data availability

Original data have been attachmentd in the paper as supplementary tables

Acknowledgments

We are grateful to the editor and two anonymous reviewers for their insightful comments, which have greatly improved the manuscript. This research was supported by the National Natural Science Foundation of China (NSFC, No. 42172204; 42011530078; 41888101; 42272214) to J.-Y. Li, T.-Y. Li, and H. Cheng, Yunnan Fundamental Research Projects (grant NO. 202201AS070022) to T.-Y. Li, and China Scholarship Council (202106990014) to Y. Wu. U–Th dating at the High-Precision Mass Spectrometry and Environment Change Laboratory (HISPEC) was supported by grants from the Science Vanguard Research Program of the Ministry of Science and Technology (MOST), Taiwan, ROC (110-2123-M-002-009 to C.-C. Shen), the Higher Education Sprout Project of the Ministry of Education, Taiwan, ROC (110L901001 to C.-C. Shen), and the National Taiwan University (110L8907 to C.-C. Shen).

Appendix A. Supplementary data

Supplementary data to this article can be found online at https://doi.org/10.1016/j.quascirev.2022.107869.

References

Andrews, J.T., Voelker, A.H.L., 2018. Heinrich events" (& sediments): a history of terminology and recommendations for future usage. Quat. Sci. Rev. 187, 31–40.
Bai, Z.H., Dong, W.J., 2004. Climate features and formation causes of autumn rain over southwest China (in Chinese). Plateau Meteorol. 23, 884–889.
Barker, S., Diz, P., Vautravers, M.J., Pike, J., Knorr, G., Hall, I.R., Broecker, W.S., 2009. Interhemispheric Atlantic seesaw response during the last deglaciation. Nature 457 (7233), 1097–1102.
Bassis, J.N., Petersen, S.V., Mac Cathles, L., 2017. Heinrich events triggered by ocean forcing and modulated by isostatic adjustment. Nature 542 (7641), 332–334.
Bauska, T.K., Marcott, S.A., Brook, E.J., 2021. Abrupt changes in the global carbon cycle during the last glacial period. Nat. Geosci. 14 (2), 91–96.
Belen, M., Grimalt, J.O., Shackleton, N.J., Lucia, D.A., Hutterli, M.A., Stocker, T.F., 2007. Four climate cycles of recurring deep and surface water destabilizations on the Iberian margin. Science 317 (5837), 502–507.
Bradley, R.S., Diaz, H.F., 2021. Late quaternary abrupt climate change in the tropics and sub-tropics: the continental signal of tropical hydroclimatic events (THEs). Rev. Geophys. 59 (4), e2020RG000732.
Breitenbach, S.F.M., Rehfeld, K., Goswami, B., Baldini, J.U.L., Ridley, H.E., Kennett, D.J., Prufer, K.M., Aquino, V.V., Asmerom, Y., Polyak, V.J., Cheng, H., Kurths, J., Marwan, N., 2012. Constructing proxy records from age models (COPRA). Clim. Past 8 (5), 1765–1779.
Broecker, W., Bond, G., Klas, M., Clark, E., McManus, J., 1992. Origin of the northern Atlantic's Heinrich events. Clim. Dynam. 6 (3), 265–273.
Brovkin, V., Brook, E., Williams, J.W., Bathiany, S., Lenton, T.M., Barton, M., DeConto, R.M., Donges, J.F., Ganopolski, A., McManus, J., Praetorius, S., de Vernal, A., Abe-Ouchi, A., Cheng, H., Claussen, M., Crucifix, M., Gallopín, G., Iglesias, V., Kaufman, D.S., Kleinen, T., Lambert, F., van der Leeuw, S., Liddy, H., Loutre, M.-F., McGee, D., Rehfeld, K., Rhodes, R., Seddon, A.W.R., Trauth, M.H., Vanderveken, L., Yu, Z., 2021. Past abrupt changes, tipping points and cascading impacts in the Earth system. Nture Geoscience 14, 550–558.
Buizert, C., Sigl, M., Severi, M., Markle, B.R., Wettstein, J.J., McConnell, J.R., Pedro, J.B., Sodemann, H., Goto-Azuma, K., Kawamura, K., Fujita, S., Motoyama, H., Hirabayashi, M., Uemura, R., Stenni, B., Parrenin, F., He, F., Fudge, T.J., Steig, E.J., 2018. Abrupt ice-age shifts in southern westerly winds and Antarctic climate forced from the north. Nature 563 (7733), 681–685.
Burns, S.J., McGee, D., Scroxton, N., Kinsley, C.W., Godfrey, L.R., Faina, P., Ranivoharimanana, L., 2022. Southern Hemisphere controls on ITCZ variability in southwest Madagascar over the past 117,000 years. Quat. Sci. Rev. 276, 107317.

Cai, Z.Y., Tian, L.D., Bowen, G.J., 2017. ENSO variability reflected in precipitation oxygen isotopes across the Asian Summer Monsoon region. Earth Planet Sci. Lett. 475, 25–33.
Cai, Z.Y., Tian, L.D., Bowen, G.J., 2018. Spatial-seasonal patterns reveal large-scale atmospheric controls on Asian Monsoon precipitation water isotope ratios. Earth Planet Sci. Lett. 503, 158–169.
Carolin, S.A., Cobb, K.M., Adkins, J.F., Clark, B., Conroy, J.L., Lejau, S., Malang, J., Tuen, A.A., 2013. Varied response of western pacific hydrology to climate forcings over the last glacial period. Science 340 (6140), 1564–1566.
Chen, C.-J., Huang, R., Yuan, D.-X., Zhang, J., Cheng, H., Ning, Y.-F., Yu, T.-L., Shen, C.-C., Edwards, R.L., Long, X.-Y., Wang, T., Xiao, S.-Y., Wu, Y., Liu, Q.-Z., Li, T.-Y., Li, J.-Y., 2021b. Karst hydrological changes during the late-holocene in southwestern China. Quat. Sci. Rev. 258. https://doi.org/10.1016/j.quascirev.2021.106865.
Chen, C., Yuan, D., Yu, T., Shen, C., Edwards, R.L., Wu, Y., Xiao, S., Zhang, J., Wang, T., Huang, R., Liu, Z., Li, T., Li, J., 2021a. Human activity and climate change triggered the expansion of rocky desertification in the karst areas of Southwestern China. Sci. China Earth Sci. 64. https://doi.org/10.1007/s11430-020-9760-7.
Chen, C.-J., Li, T.-Y., 2018. Geochemical characteristics of cave drip water respond to ENSO based on a 6-year monitoring work in Yangkou cave, Southwest China. J. Hydrol. 561, 896–907.
Cheng, H., Lawrence Edwards, R., Shen, C.-C., Polyak, V.J., Asmerom, Y., Woodhead, J., Hellstrom, J., Wang, Y.J., Kong, X.G., Spötl, C., 2013. Improvements in ^{230}Th dating, ^{230}Th and ^{234}U half-life values, and U-Th isotopic measurements by multi-collector inductively coupled plasma mass spectrometry. Earth Planet Sci. Lett. 371–372, 82–91.
Cheng, H., Xu, Y., Dong, X.Y., Zhao, J.Y., Li, H.Y., Baker, J., Sinha, A., Spötl, C., Zhang, H.W., Du, W.J., Zong, B.Y., Jia, X., Kathayat, G., Liu, D.B., Cai, Y.J., Wang, X.F., Strikis, N.M., Cruz, F.W., Auler, A.S., Gupta, A.K., Singh, R.K., Jaglan, S., Dutt, S., Liu, Z.Y., Edwards, R.L., 2021. Onset and termination of Heinrich Stadial 4 and the underlying climate dynamics. Communications Earth & Environment 2 (1), 230.
Chiang, J.C.H., Fung, I.Y., Wu, C.-H., Cai Y J, Y.J., Edman J P, J.P., Liu, Y.W., Day, J.A., Bhattacharya, T., Mondal, Y., Labrousse, C.A., 2015. Role of seasonal transitions and westerly jets in East Asian paleoclimate. Quat. Sci. Rev. 108, 111–129.
Chiang, J.C.H., Herman, M.J., Yoshimura, K., Fung, I.Y., 2020. Enriched East Asian oxygen isotope of precipitation indicates reduced summer seasonality in regional climate and westerlies. Proc. Natl. Acad. Sci. USA 117, 14745–14750.
Chiang, J.C.H., Swenson, L.M., Kong, W., 2017. Role of Seasonal Transitions and the Westerlies in the Interannual Variability of the East Asian Summer Monsoon Precipitation: Seasonal Transitions in EASM variability. Geophys. Res. Lett. 44 (8), 3788–3795.
Cosford, J., Qing, H.R., Mattey, D., Eglington, B., Zhang, M.L., 2009. Climatic and local effects on stalagmite δ^{13}C values at Lianhua Cave, China. Palaeogeogr. Palaeoclimatol. Palaeoecol. 280, 235–244.
Cruz, F.W., Burns, S.J., Jercinovic, M., Karmann, I., Sharp, W.D., Vuille, M., 2007. Evidence of rainfall variations in Southern Brazil from trace element ratios (Mg/Ca and Sr/Ca) in a Late Pleistocene stalagmite. Geochem. Cosmochim. Acta 71, 2250–2263.
Deplazes, G., Lückge, A., Peterson, L.C., Timmermann, A., Hamann, Y., Hughen, K.A., Röhl, U., Laj, C., Cane, M.A., Sigman, D.M., Haug, G.H., 2013. Links between tropical rainfall and North Atlantic climate during the last glacial period. Nat. Geosci. 6, 213.
Ding, Y.H., Si, D., Liu, Y.J., 2018. On the characteristics, driving forces and inter-decadal variability of the East Asian summer monsoon (in Chinese). J. Atmos. Sci. 42, 533–558.
Dong, J.G., Shen, C.-C., Kong, X.G., Wang, Y., Duan, F.C., 2018. Asian monsoon dynamics at Dansgaard/Oeschger events 14–8 and Heinrich events 5–4 in northern China. Quat. Geochronol. 47, 72–80.
Dong, X.Y., Kathayat, G., Rasmussen, S.O., Svensson, A., Severinghaus, J.P., Li, H.Y., Sinha, A., Xu, Y., Zhang, H.W., Shi, Z.G., Cai, Y.J., Pérez-Mejías, C., Baker, J., Zhao, J.Y., Spötl, C., Columbu, A., Ning, Y.F., Stríkis, N.M., Chen, S.T., Wang, X.F., Gupta, A.K., Dutt, S., Zhang, F., Cruz, F.W., An, Z.S., Lawrence Edwards, R., Cheng, H., 2022. Coupled atmosphere-ice-ocean dynamics during Heinrich stadial 2. Nat. Commun. 13, 5867.
Dorale, J.A., Edwards, R.L., Ito, E., González, L.A., 1998. Climate and vegetation history of the midcontinent from 75 to 25 ka: a speleothem record from crevice cave, Missouri, USA. Science 282, 1871–1874.
Dorale, J.A., Liu, Z., 2009. Limitations of Hendy test criteria in judging the paleoclimatic suitability of speleothems and the need for replication. Journal of Cave & Karst Studies the National Speleological Society Bulletin 71, 73–80.
Duan, W.H., Cheng, H., Tan, M., Edwards, R.L., 2016a. Onset and duration of transitions into Greenland Interstadials 15.2 and 14 in northern China constrained by an annually laminated stalagmite. Sci. Rep. 6, 20844.
Duan, W.H., Ruan, J.Y., Luo, W.J., Li, T.Y., Tian, L.J., Zeng, G.N., Zhang, D.Z., Bai, Y.J., Li, J.L., Tao, T., Zhang, P.Z., Baker, A., Tan, M., 2016b. The transfer of seasonal isotopic variability between precipitation and drip water at eight caves in the monsoon regions of China. Geochem. Cosmochim. Acta 183, 250–266.
Edwards, R.L., Chen, J.H., Wasserburg, G.J., 1987. ^{238}U-^{234}U-^{230}Th-^{232}Th systematics and the precise measurement of time over the past 500,000 years. Earth Planet Sci. Lett. 81, 175–192.
Fairchild, I.J., Smith, C.L., Baker, A., Fuller, L., Spötl, C., Mattey, D., McDermott, F., EIMF, 2006. Modification and preservation of environmental signals in speleothems. Earth Sci. Rev. 75, 105–153.
Fairchild, I.J., Treble, P.C., 2009. Trace elements in speleothems as recorders of environmental change. Quat. Sci. Rev. 28, 449–468.
Fohlmeister, J., Voarintsoa, N.R.G., Lechleitner, F.A., Boyd, M., Brandtstätter, S., Jacobson, M.J., Oster J, L., 2020. Main controls on the stable carbon isotope composition of speleothems. Geochem. Cosmochim. Acta 279, 67–87.
Gabitov, R.I., Sadekov, A., Leinweber, A., 2014. Crystal growth rate effect on Mg/Ca and Sr/Ca partitioning between calcite and fluid: an in situ approach. Chem. Geol. 367, 70–82.
Gkinis, V., Vinther, B.M., Popp, T.J., Quistgaard, T., Faber, A.-K., Holme, C.T., Jensen, C.-M., Lanzky, M., Lütt, A.-M., Mandrakis, V., Ørum, N.-O., Pedersen, A.-S., Vaxevani, N., Weng, Y., Capron, E., Dahl-Jensen, D., Hörhold, M., Jones, T.R., Jouzel, J., Landais, A., Masson-Delmotte, V., Oerter, H., Rasmussen, S.O., Steen-Larsen, H.C., Steffensen, J.-P., Sveinbjörnsdóttir, Á.-E., Svensson, A., Vaughn, B., White, J.W.C., 2021. A 120,000-year long climate record from a NW-Greenland deep ice core at ultra-high resolution. Sci. Data 8 (1), 141.
Guillevic, M., Bazin, L., Landais, A., Kindler, P., Orsi, A., Masson-Delmotte, V., Blunier, T., Buchardt, S.L., Capron, E., Leuenberger, M., Martinerie, P., Prié, F., Vinther, B.M., 2013. Spatial gradients of temperature, accumulation and $\delta^{18}O_{ice}$ in Greenland over a series of Dansgaard-Oeschger events. Clim. Past 9 (3), 1029–1051.
Guillevic, M., Bazin, L., Landais, A., Stowasser, C., Masson-Delmotte, V., Blunier, T., Eynaud, F., Falourd, S., Michel, E., Minster, B., Popp, T., Prié, F., Vinther, B.M., 2014. Evidence for a three-phase sequence during Heinrich Stadial 4 using a multiproxy approach based on Greenland ice core records. Clim. Past 10 (6), 2115–2133.
Hartmann, D.L., 2016. Chapter 6 - atmospheric general circulation and climate. In: Hartmann, D.L. (Ed.), Global Physical Climatology, second ed. Elsevier, Boston, pp. 159–193.
He, C.F., Liu, Z.Y., Otto-Bliesner, B.L., Brady, E.C., Zhu, C.Y., Tomas, R., Clark, P.U., Zhu, J., Jahn, A., Gu, S.F., Zhang, J., Nusbaumer, J., Noone, D., Cheng, H., Wang, Y., Yan, M., Bao, Y., 2021a. Hydroclimate footprint of pan-Asian monsoon water isotope during the last deglaciation. Sci. Adv. 7, eabe2611.
He, C.F., Liu, Z.Y., Otto-Bliesner, B.L., Brady, E.C., Zhu, C.Y., Tomas, R., Gu, S.F., Han, J., Jin, Y.S., 2021b. Deglacial variability of South China hydroclimate heavily contributed by autumn rainfall. Nat. Commun. 12 (1), 5875.
Heinrich, H., 1988. Origin and consequences of cyclic ice rafting in the northeast atlantic ocean during the past 130,000 years. Quat. Res. 29 (2), 142–152.
Hemming, S.R., 2004. Heinrich events: massive late pleistocene detritus layers of the North Atlantic and their global climate imprint. Rev. Geophys. 42 (1), RG1005.
Hendy, C.H., 1971. The isotopic geochemistry of speleothems - I. The calculation of the effects of different modes of formation on the isotopic composition of speleothems and their applicability as paleoclimatic indicators. Geochem. Cosmochim. Acta 35, 801–824.
Henry, L.G., Mcmanus, J.F., Curry, W.B., Roberts, N.L., Piotrowski, A.M., Keigwin, L.D., 2016. North Atlantic Ocean circulation and abrupt climate change during the last glaciation. Science 353 (6298), 470–474.
Herzschuh, U., Cao, X., Laepple, T., Dallmeyer, A., Telford, R.J., Ni, J., Chen, F., Kong, Z., Liu, G., Liu, K.-B., Liu, X., Stebich, M., Tang, L., Tian, F., Wang, Y., Wischnewski, J., Xu, Q., Yan, S., Yang, Z., Yu, G., Zhang, Y., Zhao, Y., Zheng, Z., 2019. Position and orientation of the westerly jet determined Holocene rainfall patterns in China. Nat. Commun. 10, 2376.
Huang, J., Wan, S.M., Li, A.C., Li, T.G., 2019. Two-phase structure of tropical hydroclimate during Heinrich Stadial 1 and its global implications. Quat. Sci. Rev. 222, 105900.
Huang, Y.M., Fairchild, I.J., 2001. Partitioning of Sr^{2+} and Mg^{2+} into calcite under karst-analogue experimental conditions. Geochem. Cosmochim. Acta 65, 47–62.
Jaffey, A.H., Flynn, K.F., Glendenin, L.E., Bentley, W.C., Essling, A.M., 1971. Precision measurement of half-lives and specific activities of ^{235}U and ^{238}U. Phys. Rev. C 4 (5), 1889–1906.
Jia, W., Zhang, P.Z., Zhang, L., Li, X., Gao, T., Wang, H., Zhang, H., Li, H., Cheng, H., Edwards, R.L., 2022. Highly resolved δ^{13}C and trace element ratios of precisely dated stalagmite from northwestern China: hydroclimate reconstruction during the last two millennia. Quat. Sci. Rev., 107473
Jiang, S.W., Zhou, X., Sachs, J.P., Luo, W.H., Tu, L.Y., Liu, X.Q., Zeng, L.Y., Peng, S.Z., Yan, Q., Liu, F., Zheng, J.Q., Zhang, J.Z., Shen, Y.N., 2021. Central eastern China hydrological changes and ENSO-like variability over the past 1800 yr. Geology 49, 1386–1390.
Jiang, X.Y., Wang, X.Y., Yang, B., He, Y.Q., Shen, C.-C., Li, Z.Z., 2014. Stalagmite-inferred abrupt climate change in the east asian monsoon at MIS 5d/5c in northern guizhou province (in Chinese). Sci. Bull. 59, 2698–2706.
Kalnay, E., Kanamitsu, M., Kistler, R., Collins, W., Deaven, D., Gandin, L., Iredell, M., Saha, S., White, G., Woollen, J., Zhu, Y., Chelliah, M., Ebisuzaki, W., Higgins, W., Janowiak, J., Mo, K.C., Ropelewski, C., Wang, J., Leetmaa, A., Reynolds, R., Jenne, R., Joseph, D., 1996. The NCEP/NCAR 40-Year Reanalysis Project. Bulletin of the American Meteorological Society 77 (3), 437–472.
Landais, A., Capron, E., Masson-Delmotte, V., Toucanne, S., Rhodes, R., Popp, T., Vinther, B., Minster, B., Prié, F., 2018. Ice core evidence for decoupling between midlatitude atmospheric water cycle and Greenland temperature during the last deglaciation. Clim. Past 14 (10), 1405–1415.
Lechleitner, F.A., Mason, A.J., Breitenbach, S.F.M., Vaks, A., Haghipour, N., Henderson, G.M., 2020. Permafrost-related hiatuses in stalagmites: evaluating the potential for reconstruction of carbon cycle dynamics. Quat. Geochronol. 56, 101037.
Li, T.-Y., 2018. False amount effect —— a discussion on one issue of isotopic climatology. Quat. Sci. 38 (6), 1545–1548 (In Chinese with English figures).

Li, C., Born, A., 2019. Coupled atmosphere-ice-ocean dynamics in Dansgaard-Oeschger events. Quat. Sci. Rev. 203, 1–20.
Li, T.-Y., Han, L.-Y., Cheng, H., Edwards, R.L., Shen, C.-C., Li, H.-C., Li, J.-Y., Huang, C.-X., Zhang, T.-T., Zhao, X., 2017. Evolution of the Asian summer monsoon during Dansgaard/Oeschger events 13–17 recorded in a stalagmite constrained by high-precision chronology from southwest China. Quat. Res. 88 (1), 121–128.
Li, T.-Y., Huang, C.-X., Tian, L.-J., Suarez, M., Gao, Y.-L., 2018. Variation of $\delta^{13}C$ in plant-soil-cave systems in karst regions with different degrees of rocky desertification in southwest China. J. Cave Karst Stud. 80, 212–228.
Li, T.-Y., Wu, Y., Shen, C.-C., Li, J.-Y., Chiang, H.-W., Lin, K., Tan, L.-C., Jiang, X.-Y., Cheng, H., Edwards, R.L., 2021a. High precise dating on the variation of the Asian summer monsoon since 37 ka BP. Sci. Rep. 11 (1), 9375.
Li, Y.D., Yang, Y., Jiang, X.Y., Zhao, J.Y., Sun, Z., Shi, X., Tian, N., Yang, Y.Y., Li, J.C., Duan, J.W., 2021b. The transport mechanism of carbon isotopes based on 10 years of cave monitoring: implications for paleoclimate reconstruction. J. Hydrol. 592, 125841.
Liang, Y.-C., Lo, M.-H., Lan, C.-W., Seo, H., Ummenhofer, C.C., Yeager, S., Wu, R.-J., Steffen, J.D., 2020. Amplified seasonal cycle in hydroclimate over the Amazon river basin and its plume region. Nat. Commun. 11 (1), 4390.
Liang, Y.J., Zhao, K., Wang, Y.J., Edwards, R.L., Cheng, H., Shao, Q.F., Chen, S.T., Wang, J.T., Zhu, J.J., 2022. Different response of stalagmite $\delta^{18}O$ and $\delta^{13}C$ to millennial-scale events during the last glacial, evidenced from Huangjin Cave, northern China. Quat. Sci. Rev. 276, 107305.
Lisiecki, L.E., Raymo, M.E., 2005. A Pliocene-Pleistocene stack of 57 globally distributed benthic delta $\delta^{18}O$ records. Paleoceanography 20, PA1003.
Liu, D.B., Wang, Y.J., Cheng, H., Edwards, R.L., Kong, X., Chen, S.T., Liu, S.S., 2018. Contrasting patterns in abrupt Asian summer monsoon changes in the last glacial period and the Holocene. Paleoceanogr. Paleoclimatol. 33, 214–226.
Liu, H.Y., Gu, Y.S., Huang, X.Y., Yu, Z.C., Xie, S.C., Cheng, S.G., 2019a. A 13,000-year peatland palaeohydrological response to the ENSO-related Asian monsoon precipitation changes in the middle Yangtze Valley. Quat. Sci. Rev. 212, 80–91.
Liu, S.F., Shi, X.F., Wong, K.-T., Chen, M.-T., Ye, W.X., Zhang, H., Cao, P., Li, J.R., Li, X.T., Khokiattiwong, S., Kornkanitnan, N., 2022. Synchronous millennial surface-stratified events with AMOC and tropical dynamic changes in the north-eastern Indian Ocean over the past 42 ka. Quat. Sci. Rev. 284, 107495.
Liu, X.K., Liu, J.B., Chen, S.Q., Chen, J.H., Zhang, X., Yan, J.J., Chen, F.H., 2020. New insights on Chinese cave $\delta^{18}O$ records and their paleoclimatic significance. Earth Sci. Rev. 207, 103216.
Liu, X.K., Liu, J.B., Shen, C.-C., Yang, Y., Chen, J.H., Chen, S.Q., Wang, X.F., Wu, C.-C., Chen, F.H., 2019b. Inconsistency between records of $\delta^{18}O$ and trace element ratios from stalagmites: evidence for increasing mid–late Holocene moisture in arid central Asia. Holocene 30, 369–379.
Liu, Z.Y., Wen, X.Y., Brady, E.C., Otto-Bliesner, B., Yu, G., Lu, H.Y., Cheng, H., Wang, Y.J., Zheng, W.P., Ding, Y.H., Edwards, R.L., Cheng, J., Liu, W., Yang, H., 2014. Chinese cave records and the east Asia summer monsoon. Quat. Sci. Rev. 83, 115–128.
McGee, D., Donohoe, A., Marshall, J., Ferreira, D., 2014. Changes in ITCZ location and cross-equatorial heat transport at the last glacial maximum, Heinrich stadial 1, and the mid-Holocene. Earth Planet Sci. Lett. 390 (4), 69–79.
McGee, D., Moreno-Chamarro, E., Green, B., Marshall, J., Galbraith, E., Bradtmiller, L., 2018. Hemispherically asymmetric trade wind changes as signatures of past ITCZ shifts. Quat. Sci. Rev. 180, 214–228.
Menviel, L., Spence, P., Yu, J., Chamberlain, M.A., Matear, R.J., Meissner, K.J., England, M.H., 2018. Southern Hemisphere westerlies as a driver of the early deglacial atmospheric CO_2 rise. Nat. Commun. 9 (1), 2503.
Merkel, U., Prange, M., Schulz, M., 2010. ENSO variability and teleconnections during glacial climates. Quat. Sci. Rev. 29, 86–100.
Mudelsee, M., 2000. Ramp function regression: a tool for quantifying climate transitions. Comput. Geosci. 26, 293–307.
Nair, A., Mohan, R., Crosta, X., Manoj, M.C., Thamban, M., Marieu, V., 2019. Southern Ocean sea ice and frontal changes during the Late Quaternary and their linkages to Asian summer monsoon. Quat. Sci. Rev. 213, 93–104.
Partin, J.W., Quinn, T.M., Shen, C.C., Okumura, Y., Cardenas, M.B., Siringan, F.P., Banner, J.L., Lin, K., Hu, H.M., Taylor, F.W., 2015. Gradual onset and recovery of the Younger Dryas abrupt climate event in the tropics. Nat. Commun. 6 (1), 8061.
Pausata, F.S.R., Battisti, D.S., Nisancioglu, K.H., Bitz, C.M., 2011. Chinese stalagmite $\delta^{18}O$ controlled by changes in the Indian monsoon during a simulated Heinrich event. Nat. Geosci. 4 (7), 474–480.
Peckover, E.N., Andrews, J.E., Leeder, M.R., Rowe, P.J., Marca, A., Sahy, D., Noble, S., Gawthorpe, R., 2019. Coupled stalagmite – alluvial fan response to the 8.2 ka event and early Holocene palaeoclimate change in Greece. Palaeogeogr. Palaeoclimatol. Palaeoecol. 532, 109252.
Pedro, J.B., Jochum, M., Buizert, C., Feng, H., Barker, S., Rasmussen, S.O., 2018. Beyond the bipolar see-saw: toward a process understanding of interhemispheric coupling. Quat. Sci. Rev. 192, 27–46.
Qiu, H.-Y., Li, T.-Y., Chen, C.-J., Huang, R., Wang, T., Wu, Y., Xiao, S.-Y., Xu, Y.-Z., Huang, Y.-Y., Zhang, J., Yang, Y., Li, J.-Y., 2021. Significance of active speleothem $\delta^{18}O$ at annual-decadal timescale——a case study from monitoring in Furong Cave. Appl. Geochem. 126, 104873.
Qiu, W.Y., Zhang, X., Jiang, X.Y., Hu, H.-M., Ma, L., Xiao, H.Y., Cai, B.G., Shen, C.-C., 2022. Double-plunge structure of the East Asian summer monsoon during Heinrich stadial 1 recorded in Xianyun Cave, southeastern China. Quat. Sci. Rev. 282, 107442.
Rae, J.W.B., Burke, A., Robinson, L.F., Adkins, J.F., Chen, T., Cole, C., Greenop, R., Li, T., Littley, E.F.M., Nita, D.C., Stewart, J.A., Taylor, B.J., 2018. CO_2 storage and release in the deep Southern Ocean on millennial to centennial timescales. Nature 562 (7728), 569–573.
Routson, C.C., McKay, N.P., Kaufman, D.S., Erb, M.P., Goosse, H., Shuman, B.N., Rodysill, J.R., Ault, T., 2019. Mid-latitude net precipitation decreased with Arctic warming during the Holocene. Nature 568, 83–87.
Ruan, J.Y., Zhang, H.Y., Cai, Z.Y., Yang, X.Q., Yin, J., 2019. Regional controls on daily to interannual variations of precipitation isotope ratios in Southeast China: implications for paleomonsoon reconstruction. Earth Planet Sci. Lett. 527, 115794.
Ruggieri, E., 2013. A Bayesian approach to detecting change points in climatic records. Int. J. Climatol. 33, 520–528.
Saikku, R., Stott, L., Thunell, R., 2009. A bi-polar signal recorded in the western tropical Pacific: northern and Southern Hemisphere climate records from the Pacific warm pool during the last Ice Age. Quat. Sci. Rev. 28 (23–24), 2374–2385.
Shen, C.-C., Lin, K., Duan, W.H., Jiang, X.Y., Partin, J.W., Edwards, R.L., Cheng, H., Tan, M., 2013. Testing the annual nature of speleothem banding. Sci. Rep. 3, 2633.
Shen, C.-C., Wu, C.-C., Cheng, H., Edwards, R.-L., Hsieh, Y.-T., Gallet, S., Hori, M., 2012. High-precision and high-resolution carbonate ^{230}Th dating by MC-ICP-MS with SEM protocols. Geochem. Cosmochim. Acta 99, 71–86.
Skinner, L., Menviel, L., Broadfield, L., Gottschalk, J., Greaves, M., 2020. Southern Ocean convection amplified past Antarctic warming and atmospheric CO_2 rise during Heinrich Stadial 4. Communications Earth & Environment 1 (1), 23.
Spötl, C., Fairchild, I., Tooth, A., 2005. Cave air control on drip water geochemistry, Obir Caves (Austria): implications for speleothem deposition in dynamically ventilated caves. Geochem. Cosmochim. Acta 69, 2451–2468.
Stocker, T., Johnsen, S., 2003. A minimum thermodynamic model for a bipolar seesaw. Paleoceanogr. Paleoclimatol. 18 (4), PA000920.
Stoll, H., Mendez-Vicente, A., Gonzalez-Lemos, S., Moreno, A., Cacho, I., Cheng, H., Edwards, R.L., 2015. Interpretation of orbital scale variability in mid-latitude speleothem $\delta^{18}O$: significance of growth rate controlled kinetic fractionation effects. Quat. Sci. Rev. 127, 215–228.
Stott, L., Poulsen, C., Lund, S., Thunell, R., 2002. Super ENSO and global climate oscillations at millennial time scales. Science 297, 222–226.
Tan, M., 2014. Circulation effect: response of precipitation $\delta^{18}O$ to the ENSO cycle in monsoon regions of China. Clim. Dynam. 42 (3), 1067–1077.
Tan, M., Baker, A., Genty, D., Smith, C., Esper, J., Cai, B., 2006. Applications of stalagmite laminae to paleoclimate reconstructions: comparison with dendrochronology/climatology. Quat. Sci. Rev. 25, 2103–2117.
Taylor, S.R., Mclennan, S.M., 1995. The geochemical evolution of the continental crust. Rev. Geophys. 33, 241–265.
Tremaine, D.M., Froelich, P.N., 2013. Speleothem trace element signatures: a hydrologic geochemical study of modern cave drip waters and farmed calcite. Geochem. Cosmochim. Acta 121, 522–545.
Urs, R., Matthias, B., Regine, R., Sepp, K., Kumiko, G.A., Hansson, M.E., Johnsen, S.J., Lu, H., Steffensen, J.P., 2007. Ice core evidence for a very tight link between North Atlantic and east Asian glacial climate. Geophys. Res. Lett. 34 (3), 116–142.
Waelbroeck, C., Pichat, S., Böhm, E., Lougheed, B.C., Faranda, D., Vrac, M., Missiaen, L., Vazquez Riveiros, N., Burckel, P., Lippold, J., Arz, H.W., Dokken, T., Thil, F., Dapoigny, A., 2018. Relative timing of precipitation and ocean circulation changes in the western equatorial Atlantic over the last 45 kyr. Clim. Past 14, 1315–1330.
WAIS Divide Project Members, 2015. Precise interpolar phasing of abrupt climate change during the last ice age. Nature 520 (7549), 661–665.
Wang, Y.M.V., Larsen, T., Lauterbach, S., Andersen, N., Blanz, T., Krebs-Kanzow, U., Gierz, P., Schneider Ralph, R., 2022a. Higher sea surface temperature in the Indian ocean during the last interglacial weakened the south asian monsoon. Proc. Natl. Acad. Sci. USA 119, e2107720119.
Wang, M., Chen, S.T., Wang, Y.J., Zhao, K., Wang, X.F., Liang, Y.J., Wang, Z.J., Zhang, Z.Q., Chen, G.Z., 2022b. Stalagmite multi-proxy evidence of wet and dry intervals in the middle Yangtze Valley during the last glacial period. Palaeogeogr. Palaeoclimatol. Palaeoecol. 586, 110764.
Wang, P.X., Wang, B., Cheng, H., Fasullo, J., Guo, Z., Kiefer, T., Liu, Z., 2017. The global monsoon across time scales: mechanisms and outstanding issues. Earth Sci. Rev. 174, 84–121.
Warken, S.F., Scholz, D., Spötl, C., Jochum, K.P., Pajón, J.M., Bahr, A., Mangini, A., 2019. Caribbean hydroclimate and vegetation history across the last glacial period. Quat. Sci. Rev. 218, 75–90.
Wassenburg, J.A., Riechelmann, S., Schröder-Ritzrau, A., Riechelmann, D.F.C., Richter, D.K., Immenhauser, A., Terente, M., Constantin, S., Hachenberg, A., Hansen, M., Scholz, D., 2020. Calcite Mg and Sr partition coefficients in cave environments: implications for interpreting prior calcite precipitation in speleothems. Geochem. Cosmochim. Acta 269, 581–596.
Weber, M.E., Clark, P.U., Kuhn, G., Timmermann, A., Sprenk, D., Gladstone, R., Zhang, X., Lohmann, G., Menviel, L., Chikamoto, M.O., Friedrich, T., Ohlwein, C., 2014. Millennial-scale variability in Antarctic ice-sheet discharge during the last deglaciation. Nature 510, 134–138.
Wendt, K.A., Häuselmann, A.D., Fleitmann, D., Berry, A.E., Wang, X., Auler, A.S., Cheng, H., Edwards, R.L., 2019. Three-phased Heinrich stadial 4 recorded in NE Brazil stalagmites. Earth Planet Sci. Lett. 510, 94–102.
Wu, Y., Li, T.-Y., Yu, T.-L., Shen, C.-C., Chen, C.-J., Zhang, J., Li, J.-Y., Wang, T., Huang, R., Xiao, S.-Y., 2020. Variation of the Asian summer monsoon since the last glacial-interglacial recorded in a stalagmite from southwest China. Quat. Sci. Rev. 234, 106261.

Xu, K., Zhu, C.W., Wang, W.Q., 2016. The cooperative impacts of the El Niño−Southern Oscillation and the Indian Ocean Dipole on the interannual variability of autumn rainfall in China. Int. J. Climatol. 36, 1987−1999.
Xue, G., Cai, Y.J., Lu, Y.B., Ma, L., Cheng, X., Liu, C.C., Yan, H., Sun, Y.B., Li, D., Wei, Y.Y., Huang, S.Y., He, M., Cheng, H., Edwards, R.L., 2021. Speleothem-based hydroclimate reconstructions during the penultimate deglaciation in northern China. Paleoceanogr. Paleoclimatol. 36, e2020PA004072.
Xue, J.B., Zhong, W., Xie, L.C., Unkel, I., 2015. Vegetation responses to the last glacial and early Holocene environmental changes in the northern Leizhou Peninsula, south China. Quat. Res. 84, 223−231.
Yan, H., Wei, W., Soon, W., An, Z.S., Zhou, W.J., Liu, Z.H., Wang, Y.H., Carter, R.M., 2015. Dynamics of the intertropical convergence zone over the western pacific during the little ice age. Nat. Geosci. 8, 315.
Yang, Q., Ma, Z.G., Fan, X.G., Yang, Z.-L., Xu, Z.F., Wu, P.L., 2017. Decadal modulation of precipitation patterns over eastern China by sea surface temperature anomalies. J. Clim. 30, 7017−7033.
Yin, J.-J., Tang, W., Wang, Z.J., Pu, J.B., Lan, G.Y., Yang, H., Wu, X., Li, J.H., 2021. Deciphering the hydroclimatic significance of dripwater $\delta^{13}C_{DIC}$ variations in monsoonal China based on modern cave monitoring. J. Hydrol. 603, 126882.
Yu, L., Furevik, T., Otterå, O.H., Gao, Y.Q., 2015. Modulation of the pacific decadal oscillation on the summer precipitation over east China: a comparison of observations to 600-years control run of bergen climate model. Clim. Dynam. 44, 475−494.
Zhang, H.B., Griffiths, M.L., Chiang, J.C.H., Kong, W.W., Wu, S.T., Atwood, A., Huang, J.H., Cheng, H., Ning, Y.F., Xie, S.C., 2018. East Asian hydroclimate modulated by the position of the westerlies during Termination I. Science 362, 580−583.
Zhang, H.B., Griffiths, M.L., Huang, J.H., Cai, Y.J., Wang, C.F., Zhang, F., Cheng, H., Ning, Y.F., Hu, C.Y., Xie, S.C., 2016. Antarctic link with East Asian summer monsoon variability during the Heinrich Stadial-Bolling interstadial transition. Earth Planet Sci. Lett. 453, 243−251.
Zhang, H.W., Cheng, H., Cai, Y.J., Spotl, C., Sinha, A., Kathayat, G., Li, H.Y., 2020. Effect of precipitation seasonality on annual oxygen isotopic composition in the area of spring persistent rain in southeastern China and its paleoclimatic implication. Clim. Past 16, 211−225.
Zhang, H.W., Cheng, H., Spötl, C., Zhang, X., Cruz, F.W., Sinha, A., Auler, A.S., Stríkis, N.M., Wang, X.f., Kathayat, G., Li, X.L., Li, H.Y., Pérez-Mejías, C., Cai, Y.J., Ning, Y.F., Edwards, R.L., 2021a. gradual south-north climate transition in the atlantic realm within the younger Dryas. Geophys. Res. Lett. 48 (8), e2021GL092620.
Zhang, H.W., Zhang, X., Cai, Y.J., Sinha, A., Spötl, C., Baker, J., Kathayat, G., Liu, Z.Y., Tian, Y., Lu, J.Y., Wang, Z.Q., Zhao, J.Y., Jia, X.X., Du, W.J., Ning, Y.F., An, Z.S., Edwards, R.L., Cheng, H., 2021b. A data-model comparison pinpoints Holocene spatiotemporal pattern of East Asian summer monsoon. Quat. Sci. Rev. 261, 106911.
Zhang, X., Jiang, X.Y., Xiao, H.Y., Cai, B.G., Yu, T.-L., Shen, C.-C., 2021c. A gradual transition into Greenland interstadial 14 in southeastern China based on a sub-decadally-resolved stalagmite record. Quat. Sci. Rev. 253, 106769.
Zhang, X., Knorr, G., Lohmann, G., Barker, S., 2017. Abrupt North Atlantic circulation changes in response to gradual CO_2 forcing in a glacial climate state. Nat. Geosci. 10 (7), 518−523.
Zhang, J., Li, T.-Y., 2019. Seasonal and interannual variations of hydrochemical characteristics and stable isotopic compositions of drip waters in Furong Cave, southwest China based on 12 years' monitoring. J. Hydrol. 527, 40−50.
Zhang, X., Qiu, W.Y., Jiang, X.Y., Hu, H.-M., Xiao, H.Y., Cai, B.G., Shen, C.-C., 2021d. Three-phase structure of the east Asia summer monsoon during Heinrich stadial 4 recorded in Xianyun cave, southeastern China. Quat. Sci. Rev. 274, 107267.
Zhao, B.Y., Huang, X.Y., Hu, J.H., Shu, J.W., Wang, W.M., Peng, P.A., 2021a. Hydroclimate variation during the Mystery interval in the east asian summer monsoon area. Quat. Sci. Rev. 266, 107075.
Zhao, C., Cheng, J., Wang, J.J., Yan, H., Leng, C.C., Zhang, C., Feng, X.P., Liu, W.G., Yang, X.D., Shen, J., 2021b. Paleoclimate significance of reconstructed rainfall isotope changes in asian monsoon region. Geophys. Res. Lett. 48, e2021GL092460.
Zhao, D.B., Wan, S.M., Lu, Z.Y., Zhai, L., Feng, X.G., Shi, X.F., Li, A.C., 2020. Response of heterogeneous rainfall variability in East Asia to Hadley circulation reorganization during the late Quaternary. Quat. Sci. Rev. 247, 106562.
Zhao, J.Y., Cheng, H., 2017. Applications of laser scanning confocal microscope to paleoclimate research: characterizing and counting lamina (in Chinese). Quat. Sci. 37 (6), 1472−1474.
Zheng, R., Liu, J.H.M., Ma, Z.F., 2018. Impacts of the summertime warm pool in the West Pacific on Huaxi autumn rain and its possible physical mechanism (in Chinese). Acta Meteorol. Sin. 76, 714−725.
Ziemen, F.A., Kapsch, M.L., Klockmann, M., Mikolajewicz, U., 2019. Heinrich events show two-stage climate response in transient glacial simulations. Clim. Past 15 (1), 153−168.